

# 1 Measuring cis-regulatory energetics 2 in living cells using allelic manifolds

3 Talitha Forcier<sup>1</sup>, Andalus Ayaz<sup>1</sup>, Manraj S. Gill<sup>1,§</sup>, Daniel Jones<sup>1,2,¶</sup>, Rob Phillips<sup>2</sup>,  
4 Justin B. Kinney<sup>1,\*</sup>

\*For correspondence:  
[jkinney@cshl.edu](mailto:jkinney@cshl.edu) (JBK)

Present address: <sup>§</sup>Department of  
Biology, Massachusetts Institute of  
Technology, USA; <sup>¶</sup>Department of  
Cell and Molecular Biology, Uppsala  
University, Sweden

5 <sup>1</sup>Simons Center for Quantitative Biology, Cold Spring Harbor Laboratory, USA;

6 <sup>2</sup>Department of Applied Physics, California Institute of Technology, USA

---

8 **Abstract** Gene expression in all organisms is controlled by cooperative interactions between  
9 DNA-bound transcription factors (TFs), but quantitatively measuring TF-DNA and TF-TF interactions  
10 remains difficult. Here we introduce a strategy for precisely measuring the Gibbs free energy of  
11 such interactions in living cells. This strategy centers on the measurement and modeling of “allelic  
12 manifolds”, a multidimensional generalization of the classical genetics concept of allelic series.  
13 Allelic manifolds are measured using reporter assays performed on strategically designed  
14 cis-regulatory sequences. Quantitative biophysical models are then fit to the resulting data. We  
15 used this strategy to study regulation by two *Escherichia coli* TFs, CRP and  $\sigma^{70}$  RNA polymerase.  
16 Doing so, we consistently obtained energetic measurements precise to  $\sim 0.1$  kcal/mol. We also  
17 obtained multiple results that deviate from the prior literature. Our strategy is compatible with  
18 massively parallel reporter assays in both prokaryotes and eukaryotes, and should therefore be  
19 highly scalable and broadly applicable.

---

## 21 Introduction

22 Cells regulate the expression of their genes in response to biological and environmental cues. A  
23 major mechanism of gene regulation in all organisms is the binding of transcription factor (TF)  
24 proteins to cis-regulatory elements encoded within genomic DNA. DNA-bound TFs interact with  
25 one another, either directly or indirectly, forming cis-regulatory complexes that modulate the  
26 rate at which nearby genes are transcribed (*Ptashne and Gann, 2002; Courey, 2008*). Different  
27 arrangements of TF binding sites within cis-regulatory sequences can lead to different regulatory  
28 programs, but the rules that govern *which* arrangements lead to *which* regulatory programs remain  
29 largely unknown. Understanding these rules, which are often referred to as “cis-regulatory grammar”  
30 (*Spitz and Furlong, 2012*), is a major challenge in modern biology.

31 Measuring the quantitative strength of interactions among DNA-bound TFs is critical for eluci-  
32 dating cis-regulatory grammar. In particular, knowing the Gibbs free energy of TF-DNA and TF-TF  
33 interactions is essential for building biophysical models that can quantitatively explain gene reg-  
34 ulation in terms of simple protein-DNA and protein-protein interactions (*Shea and Ackers, 1985;*  
35 *Bintu et al., 2005; Sherman and Cohen, 2012*). Biophysical models have proven remarkably suc-  
36 cessful at quantitatively explaining regulation by a small number of well-studied cis-regulatory  
37 sequences. Arguably, the biggest successes have been achieved in the bacterium *Escherichia coli*,  
38 particularly in the context of the *lac* promoter (*Vilar and Leibler, 2003; Kuhlman et al., 2007; Kinney*  
39 *et al., 2010; Garcia and Phillips, 2011; Brewster et al., 2014*) and the  $O_R/O_L$  control region of the  $\lambda$   
40 phage lysogen (*Ackers et al., 1982; Shea and Ackers, 1985; Cui et al., 2013*). But in both cases, this

41 quantitative understanding has required decades of focused study. New approaches for dissecting  
42 cis-regulatory energetics, approaches that are both systematic and scalable, will be needed before  
43 a general quantitative understanding of cis-regulatory grammar can be developed.

44 Here we address this need by describing a systematic experimental/modeling strategy for  
45 dissecting the biophysical mechanisms of transcriptional regulation in living cells. Our strategy  
46 centers on the concept of an “allelic manifold”. Allelic manifolds generalize the classical genetics  
47 concept of allelic series to multiple dimensions. An allelic series is a set of sequence variants  
48 that affect the same phenotype (or phenotypes) but differ in their quantitative strength. Here  
49 we construct allelic manifolds by measuring, in *multiple* experimental contexts, the phenotypic  
50 strength of each variant in an allelic series. Each variant thus corresponds to a data point in a  
51 multi-dimensional “measurement space”. If the measurement space is of high enough dimension,  
52 and if one’s measurements are sufficiently precise, these data should collapse to a lower-dimension  
53 manifold that represents the inherent phenotypic dimensionality of the allelic series. These data  
54 can then be used to infer quantitative biophysical models that describe the shape of the allelic  
55 manifold, as well as the location of each allelic variant within that manifold. As we show here,  
56 such inference allows one to determine *in vivo* values for important biophysical quantities with  
57 remarkable precision.

58 We demonstrate this strategy on a regulatory paradigm in *E. coli*: activation of the  $\sigma^{70}$  RNA  
59 polymerase holoenzyme (RNAP) by the cAMP receptor protein (CRP, also called CAP). CRP activates  
60 transcription when bound to DNA at positions upstream of RNAP ([Busby and Ebricht, 1999](#)), and  
61 the strength of these interactions is known to depend strongly on the precise nucleotide spacing  
62 between CRP and RNAP binding sites ([Gaston et al., 1990](#); [Ushida and Aiba, 1990](#)). However, the  
63 Gibbs free energies of these interactions are still largely unknown.<sup>1</sup> By measuring and modeling  
64 allelic manifolds, we systematically determined the *in vivo* Gibbs free energy ( $\Delta G$ ) of CRP-RNAP  
65 interactions that occur at a variety of different binding site spacings. These  $\Delta G$  values were  
66 consistently measured to an estimated precision of  $\sim 0.1$  kcal/mol. We also obtained  $\Delta G$  values for  
67 *in vivo* CRP-DNA and RNAP-DNA interactions, again with similar estimated precision.

68 The Results section that follows is organized into three Parts, each of which describes a different  
69 use for allelic manifolds. Part 1 focuses on measuring TF-DNA interactions, Part 2 focuses on TF-TF  
70 interactions, and Part 3 shows how to distinguish different possible mechanisms of transcriptional  
71 activation. Each Part consists of three subsections: Strategy, Demonstration, and Aside. Strategy  
72 covers the theoretical basis for the proposed use of allelic manifolds. Demonstration describes how  
73 we applied this strategy to better understand regulation by CRP and RNAP. Aside describes related  
74 findings that are interesting but somewhat tangential.

## 75 Results

### 76 Part 1. Strategy: Measuring TF-DNA interactions

77 We begin by showing how allelic manifolds can be used to measure the *in vivo* strength of TF binding  
78 to a specific DNA binding site. This measurement is accomplished by using the TF of interest as a  
79 transcriptional repressor. We place the TF binding site directly downstream of the RNAP binding  
80 site in a bacterial promoter so that the TF, when bound to DNA, sterically occludes the binding  
81 of RNAP. We then measure the rate of transcription from a few dozen variant RNAP binding sites.  
82 Transcription from each variant site is assayed in both the presence and in the absence of the TF.

83 Figure 1A illustrates a thermodynamic model ([Shea and Ackers, 1985](#); [Bintu et al., 2005](#); [Sherman and Cohen, 2012](#)) for this type of simple repression. In this model, promoter DNA can be in  
84 one of three states: unbound, bound by the TF, or bound by RNAP. Each of these three states is

<sup>1</sup>To our knowledge, only the CRP-RNAP interaction at the *lac* promoter has previously been quantitatively measured ([Kuhlman et al., 2007](#); [Kinney et al., 2010](#)).

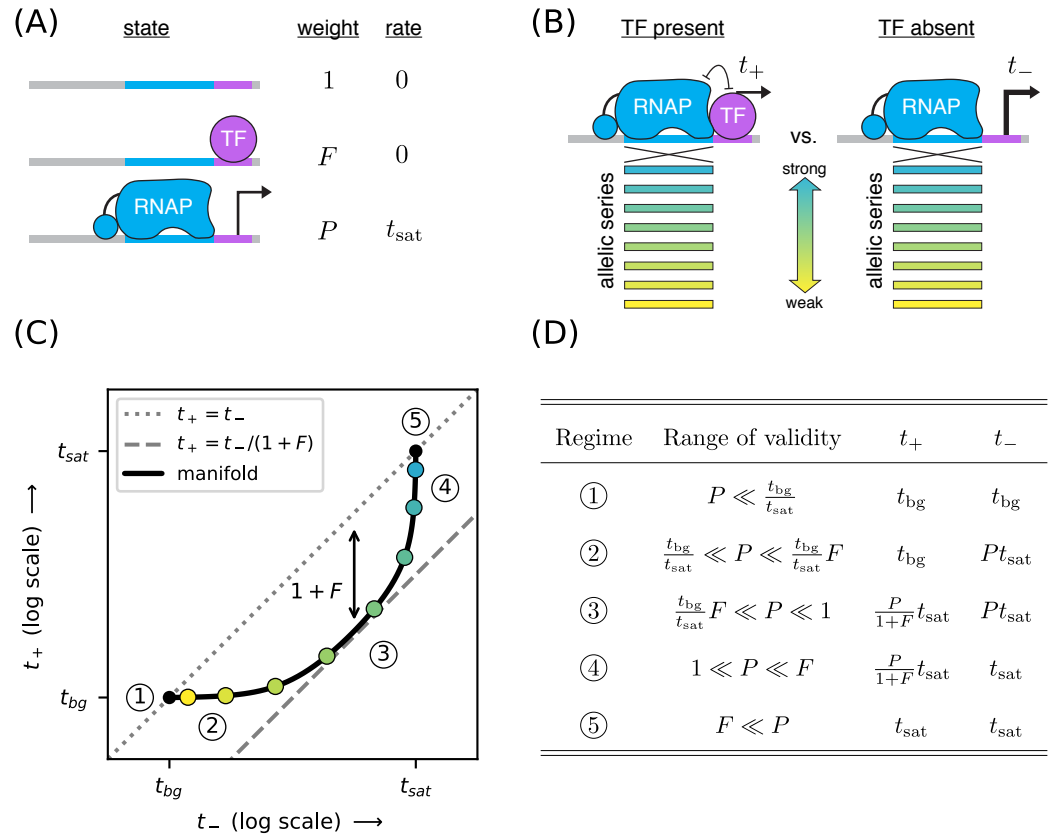


**Figure 1.** Strategy for measuring TF-DNA interactions. (A) A thermodynamic model of simple repression. Here, promoter DNA can transition between three possible states: unbound, bound by a TF, or bound by RNAP. Each state has an associated Boltzmann weight and rate of transcript initiation.  $F$  is the TF binding factor and  $P$  is the RNAP binding factor; see text for a description of how these dimensionless binding factors relate to binding affinity and binding energy.  $t_{sat}$  is the rate of specific transcript initiation from a promoter fully occupied by RNAP. (B) Transcription is measured in the presence ( $t_+$ ) and absence ( $t_-$ ) of the TF. Measurements are made for an allelic series of RNAP binding sites that differ in their binding strengths (blue-yellow gradient). (C) If the model in panel A is correct, plotting  $t_+$  vs.  $t_-$  for the promoters in panel B (colored dots) will trace out a 1D allelic manifold. Mathematically, this manifold reflects Equation 1 and Equation 2 computed over all possible values of the RNAP binding factor  $P$  while the other parameters ( $F, t_{sat}$ ) are held fixed. Note that these equations include a background transcription term  $t_{bg}$ ; it is assumed throughout that  $t_{bg} \ll t_{sat}$  and that  $t_{bg}$  is independent of RNAP binding site sequence. The resulting manifold exhibits five distinct regimes (circled numbers), corresponding to different ranges for the value of  $P$  that allow the mathematical expressions in Equations 1 and 2 to be approximated by simplified expressions. In regime 3, for instance,  $t_+ \approx t_-/(1+F)$ , and thus the manifold approximately follows a line parallel (on a log-log plot) to the diagonal but offset below it by a factor of  $1+F$  (dashed line). Data points in this regime can therefore be used to determine the value of  $F$ . (D) The five regimes of the allelic manifold, including approximate expressions for  $t_+$  and  $t_-$  in each regime, as well as the range of validity for  $P$ .

86 assumed to occur with a frequency that is consistent with thermal equilibrium, i.e., with a probability  
 87 proportional to its Boltzmann weight.

88 The energetics of protein-DNA binding determine the Boltzmann weight for each state. By  
 89 convention we set the weight of the unbound state equal to 1. The weight of the TF-bound state is  
 90 then given by  $F = [TF]K_F$  where  $[TF]$  is the concentration of the TF and  $K_F$  is the affinity constant in  
 91 inverse molar units. Similarly, the weight of the RNAP-bound state is  $P = [RNAP]K_P$ . In what follows  
 92 we refer to  $F$  and  $P$  as the “binding factors” of the TF-DNA and RNAP-DNA interactions, respectively.

93 We note that these binding factors can also be written as  $F = e^{-\Delta G_F/k_B T}$  and  $P = e^{-\Delta G_P/k_B T}$  where  
94  $k_B$  is Boltzmann's constant,  $T$  is temperature, and  $\Delta G_F$  and  $\Delta G_P$  respectively denote the Gibbs  
95 free energy of binding for the TF and RNAP. Note that each Gibbs free energy accounts for the  
96 entropic cost of pulling each protein out of solution. In what follows, we report  $\Delta G$  values in units  
97 of kcal/mol; note that  $1 \text{ kcal/mol} = 1.62 k_B T$  at  $37^\circ\text{C}$ .

98 The overall rate of transcription is computed by summing the amount of transcription produced  
99 by each state, weighting each state by the probability with which it occurs. In this case we assume  
100 the RNAP-bound state initiates at a rate of  $t_{\text{sat}}$ , and that the other states produce no transcripts. We  
101 also add a term,  $t_{\text{bg}}$ , to account for background transcription (e.g., from an unidentified promoter  
102 further upstream). The rate of transcription in the presence of the TF is thus given by

$$t_+ = t_{\text{sat}} \frac{P}{1 + F + P} + t_{\text{bg}}. \quad (1)$$

103 In the absence of the TF ( $F = 0$ ), the rate of transcription becomes

$$t_- = t_{\text{sat}} \frac{P}{1 + P} + t_{\text{bg}}. \quad (2)$$

104 Our goal is to measure the TF-DNA binding factor  $F$ . To do this, we create a set of promoter  
105 sequences where the RNAP binding site is varied (thus generating an allelic series) but the TF binding  
106 site is kept fixed. We then measure transcription from these promoters in both the presence and  
107 absence of the TF, respectively denoting the resulting quantities by  $t_+$  and  $t_-$  (Figure 1B). Our  
108 rationale for doing this is that changing the RNAP binding site sequence should, according to our  
109 model, affect only the RNAP-DNA binding factor  $P$ . All of our measurements are therefore expected  
110 to lie along a one-dimensional allelic manifold residing within the two-dimensional space of  $(t_-, t_+)$   
111 values. Moreover, this allelic manifold should follow the specific mathematical form implied by  
112 Equations 1 and 2 when  $P$  is varied and the other parameters ( $t_{\text{sat}}$ ,  $t_{\text{bg}}$ ,  $F$ ) are held fixed; see Figure  
113 1C.

114 The geometry of this allelic manifold is nontrivial. Assuming  $F \gg 1$  and  $t_{\text{bg}} \ll t_{\text{sat}}$ , there are five  
115 different regimes corresponding to different values of the RNAP binding factor  $P$ . These regimes  
116 are listed in Figure 1D and derived in Appendix 4. In regime 1,  $P$  is so small that both  $t_+$  and  $t_-$   
117 are dominated by background transcription, i.e.,  $t_+ \approx t_- \approx t_{\text{bg}}$ .  $P$  is somewhat larger in regime 2,  
118 causing  $t_-$  to be proportional to  $P$  while  $t_+$  remains dominated by background. In regime 3, both  $t_+$   
119 and  $t_-$  are proportional to  $P$  with  $t_+/t_- \approx 1/(1 + F)$ . In regime 4,  $t_-$  saturates at  $t_{\text{sat}}$  while  $t_+$  remains  
120 proportional to  $P$ . Regime 5 occurs when both  $t_+$  and  $t_-$  are saturated, i.e.,  $t_+ \approx t_- \approx t_{\text{sat}}$ .

## 121 Part 1. Demonstration: Measuring CRP-DNA binding

122 The placement of CRP immediately downstream of RNAP is known to repress transcription (*Morita*  
123 *et al., 1988*). We therefore reasoned that placing a DNA binding site for CRP downstream of  
124 RNAP would allow us to measure the binding factor of that site. Figure 2 illustrates measure-  
125 ments of the allelic manifold used to characterize the strength of CRP binding to the 22 bp site  
126 GAATGTGACCTAGATCCACATTT. This site contains the well-known consensus site, which comprises two  
127 palindromic pentamers (underlined) separated by a 6 bp spacer (*Gunasekera et al., 1992*). We  
128 performed measurements using this CRP site centered at two different locations relative to the  
129 transcription start site TSS: +0.5 bp and +4.5 bp.<sup>2</sup> To avoid influencing CRP binding strength, the  
130 -10 region of the RNAP site was kept fixed in the promoters we assayed while the -35 region of the  
131 RNAP binding site was varied (Figure 2A). Promoter DNA sequences are shown in Appendix 1 Figure  
132 1.

<sup>2</sup>The first transcribed base is, in this paper, assigned position 0 instead of the more conventional +1. Half-integer positions indicate centering between neighboring nucleotides.

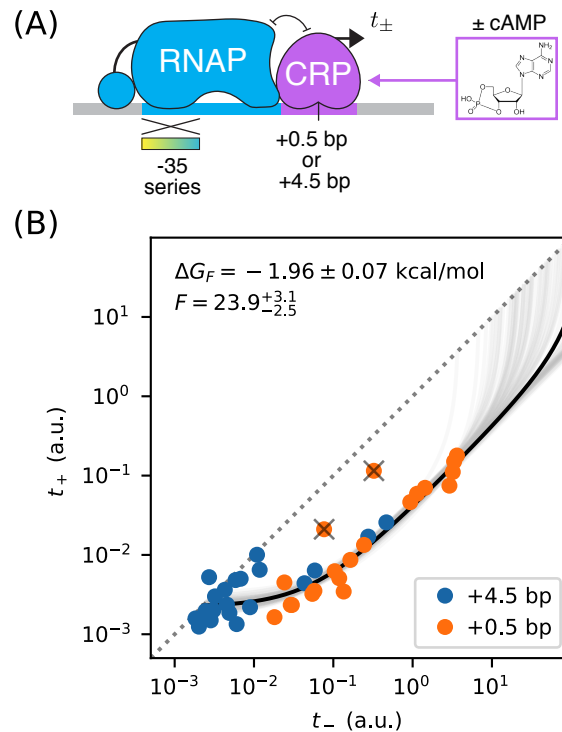


**Figure 2.** Precision measurement of *in vivo* CRP-DNA binding. (A) Expression measurements were performed on promoters for which CRP represses transcription by occluding RNAP. Each promoter assayed contained a near-consensus CRP binding site centered at either +0.5 bp or +4.5 bp, as well as an RNAP binding site with a partially mutagenized -35 region (gradient).  $t_+$  (or  $t_-$ ) denotes measurements made using *E. coli* strain JK10 grown in the presence (or absence) of the small molecule effector cAMP. (B) Dots indicate measurements for 41 such promoters. A best-fit allelic manifold (black) was inferred from  $n = 39$  of these data points after the exclusion of 2 outliers (gray 'X's). Gray lines indicate 100 plausible allelic manifolds fit to bootstrap-resampled data points. The parameters of these manifolds were used to determine the CRP-DNA binding factor  $F$  and thus the Gibbs free energy  $\Delta G_F = -k_B T \log F$ . Error bars indicate 68% confidence intervals determined by bootstrap resampling. See Appendix 3 for more information about our manifold fitting procedure.

133 We obtained  $t_-$  and  $t_+$  measurements for these constructs using a modified version of the  
 134 colorimetric  $\beta$ -galactosidase assay of [Lederberg \(1950\)](#) and [Miller \(1972\)](#); see Appendix 2 for details.  
 135 Our measurements are largely consistent with an allelic manifold having the expected mathematical  
 136 form (Figure 2B). Moreover, the measurements for promoters with CRP sites at two different  
 137 positions (+0.5 bp and +4.5 bp) appear consistent with each other, although the measurements for  
 138 +4.5 bp promoters have appear to lower values for  $P$  overall. A small number of data points do  
 139 deviate substantially from this manifold, but the presence of such outliers is not surprising from a  
 140 biological perspective (see Discussion). Fortunately, outliers appear at a rate small enough for us to  
 141 identify them by inspection.

142 We quantitatively modeled the allelic manifold in Figure 2B by fitting  $n + 3$  parameters to our  $2n$   
 143 measurements, where  $n = 39$  is the number of non-outlier promoters. The  $n + 3$  parameters were  
 144  $t_{\text{sat}}$ ,  $t_{\text{bg}}$ ,  $F$ , and  $P_1, P_2, \dots, P_n$ , where each  $P_i$  is the RNAP binding factor of promoter  $i$ . Nonlinear least  
 145 squares optimization was used to infer values for these parameters. Uncertainties in  $t_{\text{sat}}$ ,  $t_{\text{bg}}$ , and  $F$   
 146 were quantified by repeating this procedure on bootstrap-resampled data points.

147 These results yielded highly uncertain values for  $t_{\text{sat}}$  because none of our measurements appear  
 148 to fall within regime 4 or 5 of the allelic manifold. A reasonably precise value for  $t_{\text{bg}}$  was obtained,

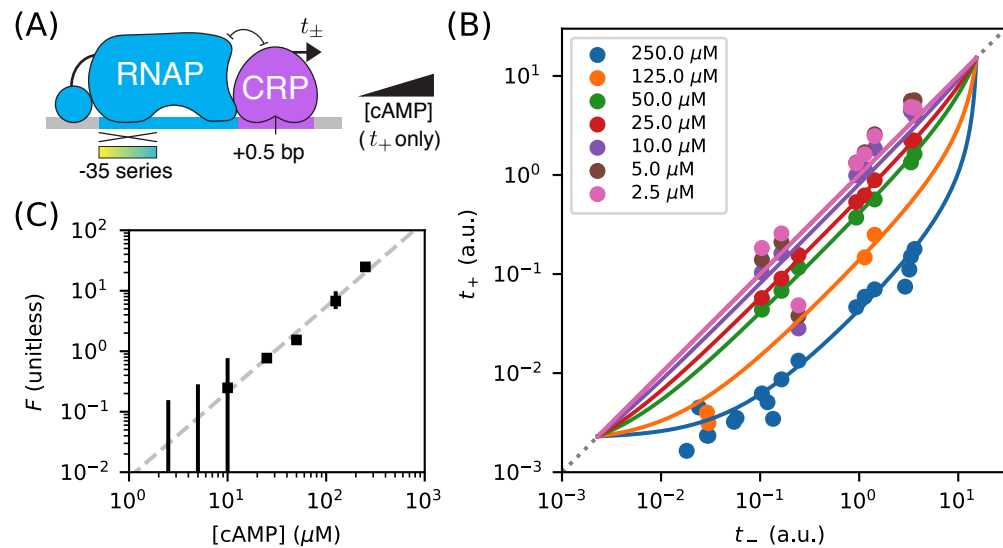


**Figure 3.** Measuring in vivo changes in TF concentration. (A) Allelic manifolds were measured for the +0.5 bp occlusion promoter architecture using seven different concentrations of cAMP (ranging from 250  $\mu\text{M}$  to 2.5  $\mu\text{M}$ ) when assaying  $t_+$ . (B) As expected, these data follow allelic manifolds that have cAMP-dependent values for the CRP binding factor  $F$ . (C) Values for  $F$  inferred from the data in panel B exhibit a nontrivial power law dependence on [cAMP]. Error bars indicate 68% confidence intervals determined by bootstrap resampling.

149 but substantial scatter about our model predictions in regime 1 and 2 remain. This scatter likely  
 150 reflects some variation in  $t_{bg}$  from promoter to promoter, variation that is to be expected since the  
 151 source of background transcription is not known and the appearance of even very weak promoters  
 152 could lead to such fluctuations.

153 These data do, however, determine a highly precise value for the strength of CRP-DNA binding:  
 154  $F = 23.9^{+3.1}_{-2.5}$  or, equivalently,  $\Delta G_F = -1.96 \pm 0.07$  kcal/mol.<sup>3</sup> This allelic manifold approach is thus able  
 155 to measure the strength of TF-DNA binding with a precision of  $\sim 0.1$  kcal/mol. For comparison, the  
 156 typical strength of a hydrogen bond in liquid water is -1.9 kcal/mol (*Markovitch and Agmon, 2007*).

157 We note that CRP forms approximately 38 hydrogen bonds with DNA when it binds to a consen-  
 158 sus DNA site (*Parkinson et al., 1996*). Our result indicates that, in living cells, the enthalpy resulting  
 159 from these and other interactions is almost exactly canceled by entropic factors. We also note that  
 160 our *in vivo* value for  $F$  is far smaller than expected from experiments in aqueous solution. The  
 161 consensus CRP binding site has been measured *in vitro* to have an affinity constant of  $K_F \sim 10^{11}$  M<sup>-1</sup>  
 162 (*Ebright et al., 1989*). There are probably about  $10^3$  CRP dimers per cell (*Schmidt et al., 2016*), giving  
 163 a concentration of [CPR]  $\sim 10^{-6}$  M. Putting these numbers together gives a binding factor of  $F \sim 10^5$ .  
 164 The nonspecific binding of CRP to genomic DNA and other molecules in the cell, and perhaps limited  
 165 DNA accessibility as well, might be responsible for this  $\sim 10^5$ -fold disagreement with our *in vivo*  
 166 measurements.

### 167 Part 1. Aside: Measuring changes in the concentration of active CRP

168 Varying cAMP concentrations in growth media changes the *in vivo* concentration of active CRP in the  
 169 *E. coli* strain we assayed (JK10). Such variation is therefore expected to alter the CRP-DNA binding  
 170 factor  $F$ . We tested whether this was indeed the case by measuring multiple allelic manifolds,  
 171 each using a different concentration of [cAMP] when measuring  $t_+$ . These measurements were  
 172 performed on promoters with CRP binding sites at +0.5 bp (Figure 3A). The resulting data are shown

<sup>3</sup>See Appendix 3 for a description of how these values and their uncertainties were computed.

173 in Figure 3B. To these data, we fit allelic manifolds having variable values for  $F$ , but fixed values for  
 174 both  $t_{\text{bg}}$  and  $t_{\text{sat}}$ .<sup>4</sup>

175 This procedure allowed us to quantitatively measure changes in the RNAP binding factor  $F$ ,  
 176 and thus changes in the *in vivo* concentration of active CRP. Our results, shown in Figure 3C,  
 177 suggest a nontrivial power law relationship between  $F$  and [cAMP]. To quantify this relationship,  
 178 we performed least squares regression ( $\log F$  against  $\log [\text{cAMP}]$ ) using data for the four largest  
 179 cAMP concentrations; measurements of  $F$  for the three other cAMP concentrations have large  
 180 asymmetric uncertainties and were therefore excluded. We found that  $F \propto [\text{cAMP}]^{1.41 \pm 0.18}$ , with  
 181 error bars representing a 95% confidence interval. We emphasize, however that our data do not  
 182 rule out a more complex relationship between [cAMP] and  $F$ .

183 There are multiple potential explanations for this deviation from proportionality. One possibility  
 184 is cooperative binding of cAMP to the two binding sites within each CRP dimer. Such cooperativity  
 185 could, for instance, result from allosteric effects like those described in [Einav et al. \(2018\)](#). Alter-  
 186 natively, this power law behavior might reflect unknown aspects of how cAMP is imported and  
 187 exported from *E. coli* cells. It is worth comparing and contrasting this result to those reported in  
 188 [Kuhlman et al. \(2007\)](#). JK10, the *E. coli* strain used in our experiments, is derived from strain TK310,  
 189 which was developed in [Kuhlman et al. \(2007\)](#). In that work, the authors concluded that  $F \propto [\text{cAMP}]$ ,  
 190 whereas our data leads us to reject this hypothesis. This illustrates one way in which using allelic  
 191 manifolds to measure how *in vivo* TF concentrations vary with growth conditions can be useful.

## 192 Part 2. Strategy: Measuring TF-RNAP interactions

193 Next we discuss how to measure an activating interaction between a DNA-bound TF and DNA-bound  
 194 RNAP. A common mechanism of transcriptional activation is “stabilization” (also called “recruitment”;  
 195 see [Ptashne \(2003\)](#)). This occurs when a DNA-bound TF stabilizes the RNAP-DNA closed complex.  
 196 Stabilization effectively increases the RNAP-DNA binding affinity  $K_p$ , and thus the binding factor  $P$ .  
 197 It does not affect  $t_{\text{sat}}$ , the rate of transcript initiation from RNAP-DNA closed complexes.

198 A thermodynamic model for activation by stabilization is illustrated in Figure 4A. Here promoter  
 199 DNA can be in four states: unbound, TF-bound, RNAP-bound, or doubly bound. In the doubly bound  
 200 state, a “cooperativity factor”  $\alpha$  contributes to the Boltzmann weight. This cooperativity factor is  
 201 related to the TF-RNAP Gibbs free energy of interaction,  $\Delta G_\alpha$ , via  $\alpha = e^{-\Delta G_\alpha/k_B T}$ . Activation occurs  
 202 when  $\alpha > 1$  (i.e.,  $\Delta G_\alpha < 0$ ). The resulting activated transcription rate is given by

$$t_+ = t_{\text{sat}} \frac{P + \alpha F P}{1 + F + P + \alpha F P} + t_{\text{bg}}. \quad (3)$$

203 This can be rewritten as

$$t_+ = t_{\text{sat}} \frac{\alpha' P}{1 + \alpha' P} + t_{\text{bg}}, \quad (4)$$

204 where

$$\alpha' = \frac{1 + \alpha F}{1 + F} \quad (5)$$

205 is a renormalized cooperativity that accounts for the strength of TF-DNA binding. As before,  $t_-$  is  
 206 given by Equation 2. Note that  $\alpha' \leq \alpha$  and that  $\alpha' \approx \alpha$  when  $F \gg 1$  and  $\alpha \gg 1/F$ .

207 As before, we measure both  $t_+$  and  $t_-$  for an allelic series of RNAP binding sites (Figure 4B).  
 208 These measurements will, according to our model, lie along an allelic manifold resembling the one  
 209 shown in Figure 4C. This allelic manifold exhibits five distinct regimes (when  $t_{\text{sat}}/t_{\text{bg}} \gg \alpha' \gg 1$ ) listed  
 210 in Figure 4D.

<sup>4</sup> $t_{\text{bg}} = 2.30 \times 10^{-3}$  a.u. was inferred in the prior analysis for Figure 2B;  $t_{\text{sat}} = 15.1$  a.u. was inferred in subsequent analysis for Figure 5C.

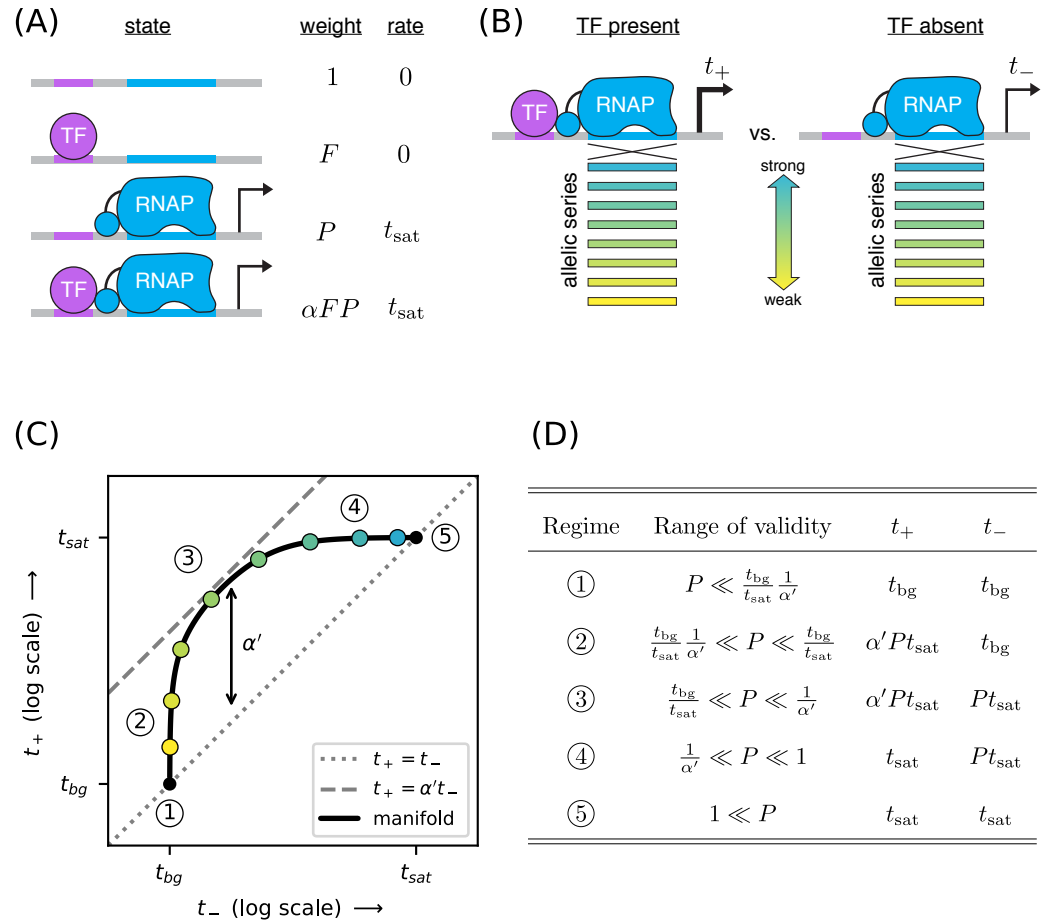


**Figure 4.** Strategy for measuring TF-RNAP interactions. (A) A thermodynamic model of simple activation. Here, promoter DNA can transition between four different states: unbound, bound by the TF, bound by RNAP, or doubly bound. As in Figure 1,  $F$  is the TF binding factor,  $P$  is the RNAP binding factor, and  $t_{\text{sat}}$  is the rate of transcript initiation from an RNAP-saturated promoter. The cooperativity factor  $\alpha$  quantifies the strength of the interaction between DNA-bound TF and RNAP molecules; see text for more information on this quantity. (B) As in Figure 1, expression is measured in the presence ( $t_+$ ) and absence ( $t_-$ ) of the TF for promoters that have an allelic series of RNAP binding sites (blue-yellow gradient). (C) If the model in panel A is correct, plotting  $t_+$  vs.  $t_-$  (colored dots) will reveal a 1D allelic manifold that corresponds to Equation 4 (for  $t_+$ ) and Equation 2 (for  $t_-$ ) evaluated over all possible values of  $P$ . Circled numbers indicate the five regimes of this manifold. In regime 3,  $t_+ \approx \alpha' t_-$  where  $\alpha'$  is the renormalized cooperativity factor given in Equation 5; data in this regime can thus be used to measure  $\alpha'$ . Separate measurements of  $F$ , using the strategy in Figure 1, then allow one to compute  $\alpha$  from knowledge of  $\alpha'$ . (D) The five regimes of the allelic manifold in panel C. Note that these regimes differ from those in Figure 1D.

## Part 2. Demonstration: Measuring class I CRP-RNAP interactions

211 CRP activates transcription at the *lac* promoter and at other promoters by binding to a 22 bp site  
 212 centered at -61.5 bp relative to the TSS. This is an example of class I activation, which is mediated  
 213 by an interaction between CRP and the C-terminal domain of one of the two RNAP  $\alpha$  subunits (the  
 214  $\alpha$ CTDs) (Busby and Ebright, 1999). *In vitro* experiments have shown this class I CRP-RNAP interaction  
 215 to activate transcription by stabilizing the RNAP-DNA closed complex.  
 216

217 We measured  $t_+$  and  $t_-$  for 47 variants of the *lac*\* promoter (see Appendix 1 Figure 1 for  
 218 sequences). These promoters have the same CRP binding site assayed for Figure 2, but positioned

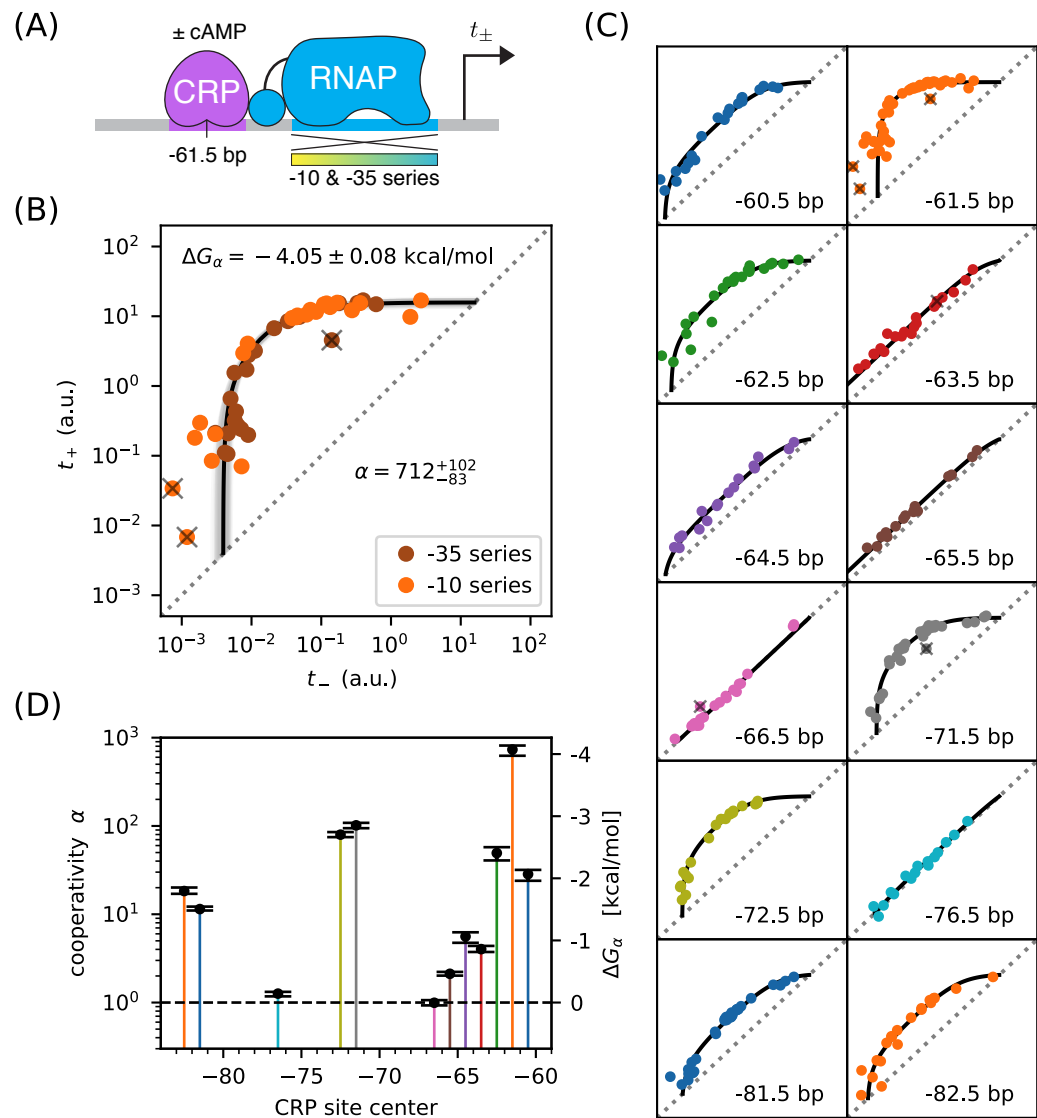


**Figure 5.** Precision measurement of class I CRP-RNAP interactions. (A)  $t_+$  and  $t_-$  were measured for promoters containing a CRP binding site centered at -61.5 bp. The RNAP sites of these promoters were mutagenized in either their -10 or -35 regions (gradient), generating two allelic series. As in Figure 2,  $t_+$  and  $t_-$  correspond to expression measurements respectively made in the presence and absence of cAMP. (B) Data obtained for 47 variant promoters having the architecture shown in panel A. Three data points designated as outliers are indicated by 'X's. The allelic manifold that best fits the  $n = 44$  non-outlier points is shown in black; 100 plausible manifolds, estimated from bootstrap-resampled data points, are shown in gray. The resulting values for  $\alpha$  and  $\Delta G_{\alpha} = -k_B T \log \alpha$  are also shown, with 68% confidence intervals indicated. (C) Allelic manifolds obtained for promoters with CRP binding sites centered at a variety of class I positions. (D) Inferred values for the cooperativity factor  $\alpha$  and corresponding Gibbs free energy  $\Delta G_{\alpha}$  for the 12 different promoter architectures assayed in panel C. Error bars indicate 68% confidence intervals. Numerical values for  $\alpha$  and  $\Delta G_{\alpha}$  at all of these class I positions are provided in Table 2.

219 at -61.5 bp relative to the TSS (Figure 5A). They differ from one another in the -10 or -35 regions of  
 220 their RNAP binding sites. Figure 5B shows the resulting measurements. With the exception of 3  
 221 outlier points, these measurements appear consistent with stabilizing activation via a Gibbs free

222 energy of  $\Delta G_\alpha = -4.05 \pm 0.08$  kcal/mol, corresponding to a cooperativity of  $\alpha = 712^{+102}_{-83}$ . We note that,  
 223 with  $F = 23.9$  determined in Figure 2B,  $\alpha' = \alpha$  to 4% accuracy.

224 This observed cooperativity is substantially stronger than suggested by previous work. Early *in*  
 225 *vivo* experiments suggested a much lower cooperativity value, e.g. 50-fold ([Beckwith et al., 1972](#)), 20-  
 226 fold ([Ushida and Aiba, 1990](#)), or even 10-fold ([Gaston et al., 1990](#)). These previous studies, however,  
 227 only measured the ratio  $t_+/t_-$  for a specific choice of RNAP binding site. This ratio is (by Equation  
 228 4) always less than  $\alpha$  and the differences between these quantities can be substantial. However,  
 229 even studies that have used explicit biophysical modeling have determined lower cooperativity  
 230 values: [Kuhlman et al. \(2007\)](#) reported a cooperativity of  $\alpha \approx 240$  ( $\Delta G_\alpha \approx -3.4$  kcal/mol), while  
 231 [Kinney et al. \(2010\)](#) reported  $\alpha \approx 220$  ( $\Delta G_\alpha \approx -3.3$  kcal/mol). Both of these studies, however, relied  
 232 on the inference of complex biophysical models with many parameters. The allelic manifold in  
 233 Figure 4, by contrast, is characterized by only three parameters ( $t_{\text{sat}}$ ,  $t_{\text{bg}}$ ,  $\alpha'$ ), all of which can be  
 234 approximately determined by visual inspection.

235 To test the generality of this approach, we measured allelic manifolds for 11 other potential  
 236 class I promoter architectures. At every one of these positions we clearly observed the collapse of  
 237 data to a 1D allelic manifold of the expected shape (Figure 5C). We then modeled these data using  
 238 values of  $\alpha$  and  $t_{\text{bg}}$  that depend on CRP binding site location, as well as a single overall value for  $t_{\text{sat}}$ .  
 239 The resulting values for  $\alpha$  (and equivalently  $\Delta G_\alpha$ ) are shown in Figure 5D and reported in Table 2. As  
 240 first shown by [Gaston et al. \(1990\)](#) and [Ushida and Aiba \(1990\)](#),  $\alpha$  depends strongly on the spacing  
 241 between the CRP and RNAP binding sites. In particular,  $\alpha$  exhibits a strong  $\sim 10.5$  bp periodicity  
 242 reflecting the helical twist of DNA. However, as with the measurement in Figure 5B, the  $\alpha$  values we  
 243 measure are far larger than the  $t_+/t_-$  ratios previously reported by [Gaston et al. \(1990\)](#) and [Ushida](#)  
 244 [and Aiba \(1990\)](#); see Table 2. We also find  $t_{\text{sat}} = 15.1^{+0.6}_{-0.5}$  a.u.. The single-cell observations of [So et al.](#)  
 245 ([2011](#)) suggest that this corresponds to  $13.8 \pm 6.6$  transcripts per minute.<sup>5</sup>

<sup>5</sup>By pure coincidence, the “arbitrary unit” (a.u.) units we use in this paper correspond very closely to “transcripts per minute”.

**Table 1.** Summary of results for class I activation by CRP. The  $\alpha$  and  $\Delta G_\alpha$  values listed here correspond to the values plotted in Figure 5D. The corresponding value inferred for the saturated transcription rate is  $t_{\text{sat}} = 15.1^{+0.6}_{-0.5}$  a.u.. Error bars indicate 68% confidence intervals; see Appendix 3 for details.  $n$  is the number of data points used to infer these values, while “outliers” is the number of data points excluded in this analysis. For comparison we show the fold-activation measurements (i.e.,  $t_+/t_-$ ) reported in [Gaston et al. \(1990\)](#) and [Ushida and Aiba \(1990\)](#); ‘-’ indicates that no measurement was reported for that position.

position (bp)	$n$	outliers	$\Delta G_\alpha$ (kcal/mol)	$\alpha$	$t_+/t_-$ (Gaston)	$t_+/t_-$ (Ushida)
-60.5	21	0	$-2.09 \pm 0.08$	$29.6^{+4.7}_{-3.5}$	3.85	-
-61.5	44	3	$-4.10 \pm 0.08$	$763^{+113}_{-84}$	9.05	20.6
-62.5	23	0	$-2.43 \pm 0.11$	$51.4^{+9.0}_{-8.5}$	4.22	-
-63.5	20	1	$-0.88 \pm 0.05$	$4.15^{+0.30}_{-0.37}$	-	-
-64.5	17	0	$-1.08 \pm 0.08$	$5.80^{+0.89}_{-0.67}$	-	-
-65.5	17	0	$-0.48 \pm 0.03$	$2.16^{+0.10}_{-0.11}$	-	-
-66.5	19	1	$0.00 \pm 0.04$	$0.99^{+0.07}_{-0.07}$	0.78	0.84
-71.5	35	1	$-2.88 \pm 0.04$	$105^{+7}_{-7}$	2.50	16.4
-72.5	20	0	$-2.73 \pm 0.04$	$83.0^{+5.2}_{-5.8}$	3.49	-
-76.5	16	0	$-0.15 \pm 0.04$	$1.27^{+0.09}_{-0.06}$	0.54	-
-81.5	32	0	$-1.53 \pm 0.03$	$11.9^{+0.4}_{-0.8}$	-	-
-82.5	20	0	$-1.82 \pm 0.05$	$19.0^{+1.3}_{-1.8}$	-	6.99

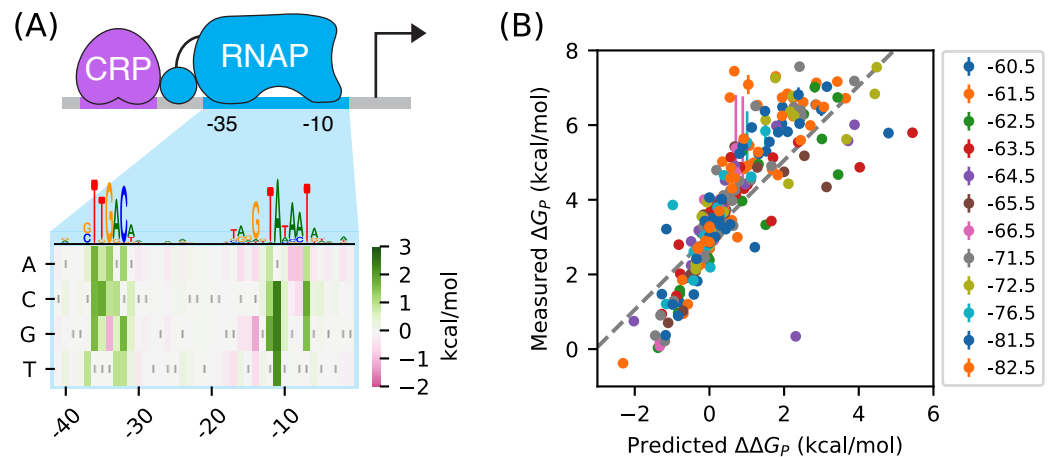


**Figure 6.** RNAP-DNA binding energy cannot be accurately predicted from sequence. (A) The PSAM for RNAP-DNA binding inferred by [Kinney et al. \(2010\)](#). This model assumes that the DNA base pair at each position in the RNAP binding site contributes independently to  $\Delta G_p$ . Shown are the  $\Delta\Delta G_p$  values assigned by this model to mutations away from the lac\* RNAP site. The sequence of the lac\* RNAP site is indicated by gray vertical bars; see also Appendix 1 Figure 1. A sequence logo representation for this PSAM is provided for reference. (B) PSAM predictions plotted against the values of  $\Delta G_p = -k_B T \log P$  inferred by fitting the allelic manifolds in Figure 5C. Error bars on these measurements represent 68% confidence intervals. Note that measured  $\Delta G_p$  values are absolute, whereas the  $\Delta\Delta G_p$  predictions of the PSAM are relative to the lac\* RNAP site, which thus corresponds to  $\Delta\Delta G_p = 0$  kcal/mol.

## Part 2. Aside: Difficulties predicting binding affinity from DNA sequence.

246 The measurement and modeling of allelic manifolds sidesteps the need to parametrically model  
247 how protein-DNA binding affinity depends on DNA sequence. In modeling the allelic manifolds in  
248 Figure 5C, we obtained values for the RNAP binding factor,  $P = [\text{RNAP}]K_p$ , for each variant RNAP  
249 binding site from the position of the corresponding data point along the length of the manifold.  
250

251 RNAP has a very well established sequence motif ([McClure et al., 1983](#)). Indeed, its DNA binding  
252 requirements were among the first characterized for any DNA-binding protein ([Pribnow, 1975](#)).  
253 More recently, a high-resolution model for RNAP-DNA binding energy was determined using data  
254 from a massively parallel reporter assay called Sort-Seq ([Kinney et al., 2010](#)). This position-specific  
255 affinity matrix (PSAM)<sup>6</sup> assumes that the nucleotide at each position contributes additively to the  
256 overall binding energy (Figure 6). This model is consistent with previously described RNAP binding  
257 motifs but, unlike those motifs, it can predict binding energy in physically meaningful energy units  
258 (i.e., kcal/mol). In what follows we denote these binding energies as  $\Delta\Delta G_p$ , because they describe  
259 differences in the Gibbs free energy of binding between two DNA sites.

260 There is good reason to believe this PSAM to be the most accurate current model of RNAP-DNA  
261 binding. However, subsequent work has suggested that the predictions of this model might still  
262 have substantial inaccuracies ([Brewster et al., 2012](#)). To investigate this possibility, we compared  
263 our measured values for the Gibbs free energy of RNAP-DNA binding ( $\Delta G_p = -k_B T \log P$ ) to binding  
264 energies ( $\Delta\Delta G$ ) predicted using the PSAM from [Kinney et al. \(2010\)](#). These values are plotted against  
265 one another in Figure 6B. Although there is a strong correlation between the predictions of the  
266 model and our measurements, deviations of 1 kcal/mol or larger (corresponding to variations in  $P$   
267 of 5-fold or greater) are not uncommon. Model predictions also systematically deviate from the  
268 diagonal, suggesting inaccuracy in the overall scale of the PSAM.

<sup>6</sup>The term PSAM comes from [Foat et al. \(2006\)](#). These models are called “energy matrices” in [Kinney et al. \(2010\)](#) and [Belliveau et al. \(2018\)](#).

269 This finding is sobering: even for one of the best understood DNA-binding proteins in biology,  
270 our best sequence-based predictions of *in vivo* protein-DNA binding affinity are still quite crude.  
271 When used in conjunction with thermodynamic models, as in [Kinney et al. \(2010\)](#), the inaccuracies  
272 of these models can have major effects on predicted transcription rates. The measurement and  
273 modeling of allelic manifolds sidesteps the need to parametrically model such binding energies,  
274 enabling the direct inference of Gibbs free energy values for each assayed RNAP binding site.

### 275 **Part 3. Strategy: Distinguishing mechanisms of transcriptional activation**

276 *E. coli* TFs can regulate multiple different steps in the transcript initiation pathway ([Lee et al., 2012](#);  
277 [Browning and Busby, 2016](#)). For example, instead of stabilizing RNAP binding to DNA, TFs can  
278 activate transcription by increasing the rate at which DNA-bound RNAP initiates transcription ([Roy  
279 et al., 1998](#)), a process we refer to as “acceleration”. CRP, in particular, has previously been reported  
280 to activate transcription in part by acceleration when positioned appropriately with respect to RNAP  
281 ([Niu et al., 1996](#); [Rhodius et al., 1997](#)).

282 We investigated whether allelic manifolds might be used to distinguish activation by acceleration  
283 from activation by stabilization. First we generalized the thermodynamic model in Figure 4A to  
284 accommodate both  $\alpha$ -fold stabilization and  $\beta$ -fold acceleration (Figure 7A). This is accomplished by  
285 using the same set of states and Boltzmann weights as in the model for stabilization, but assigning  
286 a transcription rate  $\beta t_{\text{sat}}$  (rather than just  $t_{\text{sat}}$ ) to the TF-RNAP-DNA ternary complex. The resulting  
287 activated rate of transcription is given by

$$t_+ = t_{\text{sat}} \frac{P}{1 + F + P + \alpha FP} + \beta t_{\text{sat}} \frac{\alpha FP}{1 + F + P + \alpha FP} + t_{\text{bg}}. \quad (6)$$

288 This simplifies to

$$t_+ = \beta' t_{\text{sat}} \frac{\alpha' P}{1 + \alpha' P} + t_{\text{bg}}, \quad (7)$$

289 where  $\alpha'$  is the same as in Equation 5 and

$$\beta' = \frac{1 + \alpha\beta F}{1 + \alpha F} \quad (8)$$

290 is a renormalized version of the acceleration rate  $\beta$ . The resulting allelic manifold is illustrated in  
291 Figure 7C. Like the allelic manifold for stabilization, this manifold has up to five distinct regimes  
292 corresponding to different values of  $P$  (Figure 7D). Unlike the stabilization manifold however,  $t_+ \neq t_-$   
293 in the strong RNAP binding regime (regime 5); rather,  $t_+ \approx \beta' t_{\text{sat}}$  while  $t_- \approx t_{\text{sat}}$ .

### 294 **Part 3. Demonstration: Mechanisms of class I activation by CRP**

295 We asked whether class I activation by CRP has an acceleration component. Previous *in vitro* work  
296 had suggested that the answer is ‘no’ ([Malan et al., 1984](#); [Busby and Ebright, 1999](#)), but our allelic  
297 manifold approach allows us to address this question *in vivo*. We proceeded by assaying promoters  
298 containing variant alleles of the consensus RNAP binding site (Figure 8A). Note that the consensus  
299 RNAP site is 1 bp shorter than the lac\* RNAP site (Appendix 1, Figure 1C versus Figure 1B). We  
300 therefore positioned the CRP binding site at -60.5 bp in order to realize the same spacing between  
301 CRP and the -35 element of the RNAP binding site that was realized in -61.5 bp non-consensus  
302 promoters.

303 The resulting data (Figure 8B) are seen to largely fall along the previously measured all-stabilization  
304 allelic manifold in Figure 5B. In particular, many of these data points lie at the intersection of this  
305 manifold with the  $t_+ = t_-$  diagonal. We thus find that  $\beta \approx 1$  for CRP at -61.5 bp. To further quantify  
306 possible  $\beta$  values, we fit the acceleration model in Figure 7 to each dataset shown in Figure 5B,  
307 assuming a fixed value of  $t_{\text{sat}} = 15.1$  a.u.. The resulting inferred values for  $\beta$ , shown in Figure 8C,  
308 indicate little if any deviation from  $\beta = 1$ . Our high-precision *in vivo* results therefore substantiate  
309 the previous *in vitro* results of [Malan et al. \(1984\)](#) regarding the mechanism of class I activation.

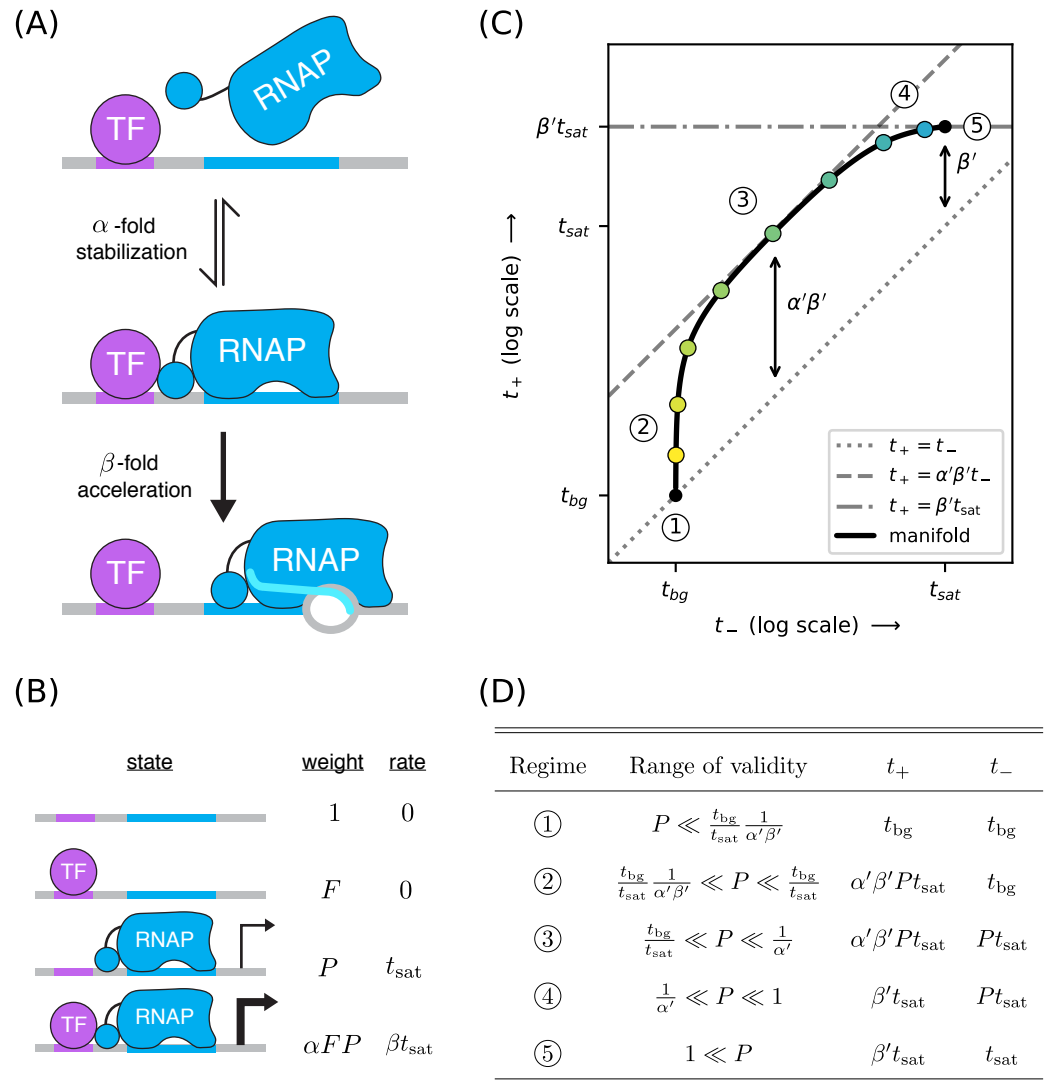


**Figure 7.** A strategy for distinguishing two different mechanisms of transcriptional activation. (A) A TF can activate transcription in two ways: (i) by stabilizing the RNAP-DNA complex or (ii) by accelerating the rate at which this complex initiates transcripts. (B) A thermodynamic model for the dual mechanism of transcriptional activation illustrated in panel A. Note that  $\alpha$  multiplies the Boltzmann weight of the doubly bound complex, whereas  $\beta$  multiplies the transcript initiation rate of this complex. (C) Data points measured as in Figure 4C will lie along a 1D allelic manifold having the form shown here. This manifold is computed using  $t_+$  values from Equation 7 and  $t_-$  values from Equation 2. Note that regime 5 occurs at a point positioned  $\beta'$ -fold above the diagonal, where  $\beta'$  is related to  $\beta$  through Equation 8. Measurements in or near the strong promoter regime ( $P \gtrsim 1$ ) can thus be used to determine the value of  $\beta'$  and, consequently, the value of  $\beta$ . (D) The five regimes of this allelic manifold are listed.

### 310 Part 3. Aside: Surprises in class II regulation by CRP

311 Many *E. coli* TFs participate in what is referred to as class II activation ([Browning and Busby, 2016](#)).  
 312 This type of activation occurs when the TF binds to a site that overlaps the -35 element (often com-  
 313 pletely replacing it) and interacts directly with the main body of RNAP. CRP is known to participate  
 314 in class II activation at many promoters ([Keseler et al., 2011](#); [Salgado et al., 2013](#)), including the

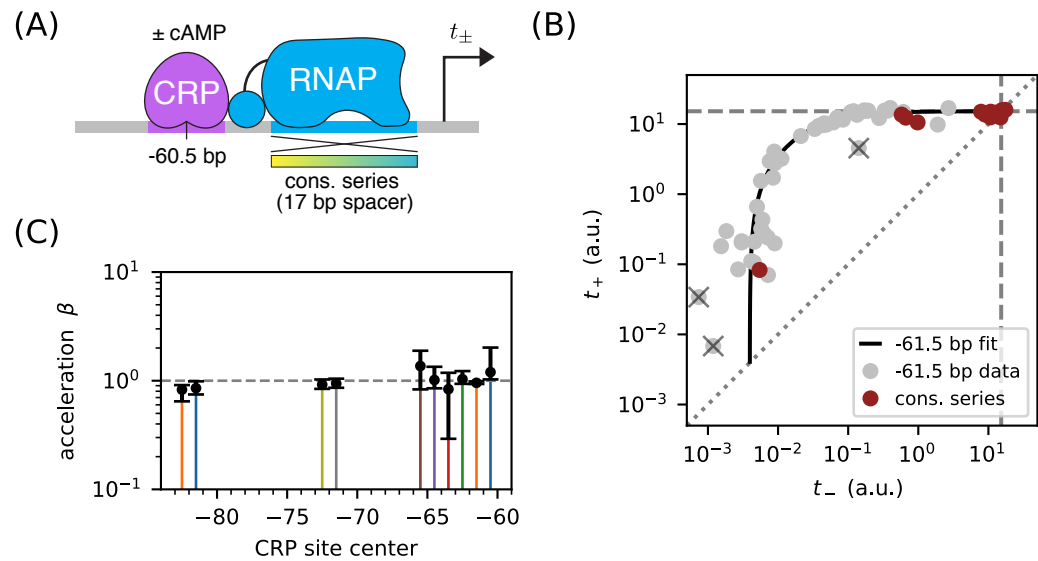


**Figure 8.** Class I activation by CRP occurs exclusively through stabilization. (A)  $t_+$  and  $t_-$  were measured for promoters containing variants of the consensus RNAP binding site as well as a CRP binding site centered at -60.5 bp. Because the consensus RNAP site is 1 bp shorter than the RNAP site of the lac\* promoter, CRP at -60.5 bp here corresponds to CRP at -61.5 bp in Figure 5. (B)  $n = 18$  data points obtained for the constructs in panel A, overlaid on the measurements from Figure 5B (gray). The value  $t_{sat} = 15.1$  a.u., inferred for Figure 5C, is indicated by dashed lines. (C) Values for  $\beta$  inferred using the data in Figure 5 for the 10 CRP positions that exhibited greater than 2-fold inducibility;  $\beta$  values at the two other CRP positions (-66.5 bp and -76.5 bp) were highly uncertain and are not shown. Error bars indicate 68% confidence intervals.

galP1 promoter, where it binds to a site centered at position -41.5 bp (Adhya, 1996). *In vitro* studies have shown CRP to activate transcription at -41.5 bp relative to the TSS through a combination of stabilization and acceleration (Niu et al., 1996; Rhodius et al., 1997).

We sought to reproduce this finding *in vivo* by measuring allelic manifolds. We therefore placed a consensus CRP site at -41.5 bp, replacing much of the -35 element in the process, and partially mutated the -10 element of the RNAP binding site (Figure 9A). Surprisingly, we observed that the resulting allelic manifold saturates at the same  $t_{sat}$  value shared by all class I promoters. Thus, CRP appears to activate transcription *in vivo* solely through stabilization, and not at all through acceleration, when located at -41.5 bp relative to the TSS (Figure 9B).

The genome-wide distribution of CRP binding sites suggests that CRP also participates in class II activation when centered at -40.5 bp (Keseler et al., 2011; Salgado et al., 2013). When assaying this promoter architecture, however, we obtained a scatter of 2D points that did not collapse to any discernible 1D allelic manifold (Figure 9D). Some of these promoters exhibit activation, some exhibit repression, and some exhibit no regulation by CRP.

These observations complicate the current understanding of class II regulation by CRP. Our *in vivo* measurements of CRP at -41.5 bp call into question the mechanism of activation previously discerned using *in vitro* techniques. The scatter observed when CRP is positioned at -40.5 bp suggests that, at this position, the -10 region of the RNAP binding site influences the values of at least two relevant biophysical parameters (not just  $P$ , as our model predicts). A potential explanation for both observations is that, because CRP and RNAP are so intimately positioned at class II promoters, even minor changes in their relative orientation caused by differences between *in vivo* and *in vitro* conditions or by changes in RNAP site sequence could have a major effect on CRP-RNAP interactions. Such sensitivity would not be expected to occur in class I activation, due to

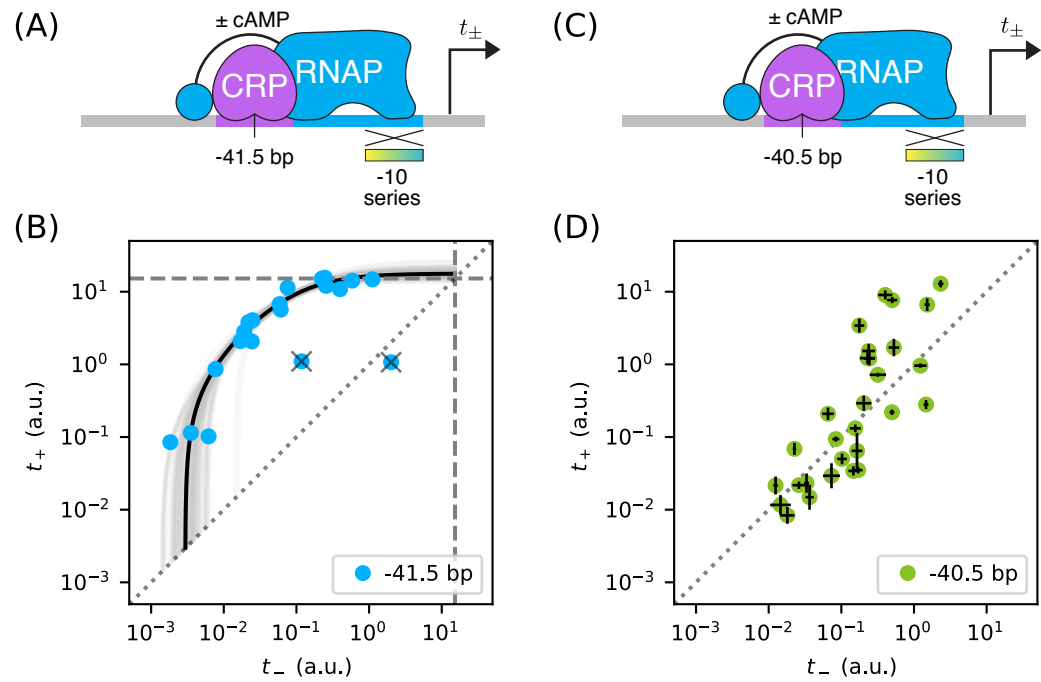


**Figure 9.** Surprises in class II regulation by CRP. (A) Regulation by CRP centered at -41.5 bp was assayed using an allelic series of RNAP binding sites that have variant -10 elements (gradient). (B) The observed allelic manifold plateaus at the value of  $t_{sat} = 15.1$  a.u. (dashed lines) determined for Figure 5B, thus indicating no detectable acceleration by CRP. This lack of acceleration is at odds with prior *in vitro* studies (Niu *et al.*, 1996; Rhodius *et al.*, 1997). (C) Regulation by CRP centered at -40.5 bp was assayed in an analogous manner. (D) Unexpectedly, data from the promoters in panel C do not collapse to a 1D allelic manifold. This finding falsifies the biophysical models in Figures 4A and 7B and indicates that CRP can either activate or repress transcription from this position, depending on as-yet-unidentified features of the RNAP binding site. Error bars in panel D indicate 95% confidence intervals estimated from replicate experiments.

338 the flexibility with which the RNAP  $\alpha$ CTDs are tethered to the core complex of RNAP.

### 339 Discussion

340 We have shown how the measurement and quantitative modeling of allelic manifolds can be used  
 341 to dissect cis-regulatory biophysics in living cells. This approach was demonstrated in *E. coli* in  
 342 the context of transcriptional regulation by two well-characterized TFs: RNAP and CRP. Here we  
 343 summarize our primary findings. We then address some caveats and limitations of the work  
 344 reported here. Finally, we elaborate on how future studies might be able to scale up this approach  
 345 using massively parallel reporter assays (MPRAs), including for studies in eukaryotic systems.

### 346 Summary

347 In each of our experiments, we quantitatively measured transcription from an allelic series of  
 348 variant RNAP binding sites, each site embedded in a fixed promoter architecture. Two expression  
 349 measurements were made for each variant promoter:  $t_+$  was measured in the presence of the  
 350 active form of CRP, while  $t_-$  was measured in the absence of active CRP. This yielded a data point,  
 351  $(t_-, t_+)$ , in a two-dimensional measurement space. We had expected the data points thus obtained  
 352 for each allelic series to collapse to a 1D curve (the allelic manifold), with different positions along  
 353 this manifold corresponding to different values of RNAP-DNA binding affinity. Such collapse was

354 indeed observed in all but one of the promoter architectures we studied. By fitting the parameters  
355 of quantitative biophysical models to these data, we obtained *in vivo* values for the Gibbs free  
356 energy ( $\Delta G$ ) of a variety of TF-DNA and TF-TF interactions.

357 In Part 1, we showed how measuring allelic manifolds for promoters in which a DNA-bound TF  
358 occludes RNAP can allow one to precisely measure the  $\Delta G$  of TF-DNA binding. We demonstrated  
359 this strategy on promoters where CRP occludes RNAP, thereby obtaining the  $\Delta G$  for a CRP binding  
360 site that was used in subsequent experiments. As an aside, we demonstrated how performing such  
361 measurements in different concentrations of the small molecule cAMP allowed us to quantitatively  
362 measure *in vivo* changes in active CRP concentration.

363 In Part 2, we showed how allelic manifolds can be used to measure the  $\Delta G$  of TF-RNAP inter-  
364 actions. We used this strategy to measure the stabilizing interactions by which CRP up-regulates  
365 transcription at a variety of class I promoter architectures. Our strategy consistently yielded  $\Delta G$   
366 values with an estimated precision of  $\sim 0.1$  kcal/mol. As an aside, we showed how  $\Delta G$  values for  
367 RNAP-DNA binding could also be obtained from these data. Notably, these  $\Delta G$  measurements for  
368 RNAP-DNA binding were seen to deviate substantially from sequence-based predictions using an  
369 established position-specific affinity matrix (PSAM) for RNAP. This highlights just how difficult it can  
370 be to accurately predict TF-DNA binding affinity from DNA sequence.

371 In Part 3, we showed how allelic manifolds can allow one to distinguish between two potential  
372 mechanisms of transcriptional activation: “stabilization” (a.k.a. “recruitment”) and “acceleration”.  
373 Applying this approach to the data from Part 2, we confirmed (as expected) that class I activation by  
374 CRP does indeed occur through stabilization and not acceleration. As an aside, we pursued this  
375 approach at two class II promoters. In contrast to prior *in vitro* studies ([Niu et al., 1996](#); [Rhodius  
376 et al., 1997](#)), no acceleration was observed when CRP was positioned at -41.5 bp relative to the TSS.  
377 Even more unexpectedly, no 1D allelic manifold was observed at all when CRP was positioned at  
378 -40.5 bp. This last finding indicates that the variant RNAP binding sites we assayed control at least  
379 one functionally important biophysical quantity in addition to RNAP-DNA binding affinity.

### 380 **Caveats and limitations**

381 An important caveat is that our  $\Delta G$  measurements assume that the *true* transcription rates (of which  
382 we obtain only noisy measurements) exactly fall along a 1D allelic manifold of the hypothesized  
383 mathematical form. These assumptions are well-motivated by the data collapse that we observed  
384 for all except one promoter architecture. But for some promoter architectures, there were a small  
385 number of “outlier” data points that we judged (by eye) to deviate substantially from the inferred  
386 allelic manifold. The presence of a few outliers makes sense biologically: The random mutations  
387 we introduced into variant RNAP binding sites will, with some nonzero probability, either shift  
388 the position of the RNAP site or create a new binding site for some other TF. However, even for  
389 promoters that exhibit clear clustering of 2D data around a 1D curve, the deviations of individual  
390 non-outlier data points from our inferred allelic manifold were often substantially larger than the  
391 experimental noise that we estimated from replicates. It may be that the biological cause of outliers  
392 is not qualitatively different from what causes these smaller but still detectable deviations from our  
393 assumed model.

394 The low-throughput experimental approach we pursued here also has important limitations.  
395 Each of the 448 variant promoters for which we report data was individually catalogued, sequenced,  
396 and assayed in at least three replicate experiments for both  $t_+$  and  $t_-$ . We opted to use a low-  
397 throughput colorimetric assay of  $\beta$ -galactosidase activity ([Lederberg, 1950](#); [Miller, 1972](#)) because  
398 this approach is well established in *E. coli* to produce a quantitative measure of transcription with  
399 high precision and high dynamic range. Such assays have also been used by other groups to  
400 develop sophisticated biophysical models of transcriptional regulation ([Kuhlman et al., 2007](#); [Cui  
401 et al., 2013](#)). However, this low-throughput approach has limited utility because it cannot be readily

402 scaled up.

403 Our reliance on cAMP as a small molecule effector of CRP presents a second limitation. In  
404 our experiments, we controlled the *in vivo* activity of CRP by growing a specially designed strain  
405 of *E. coli* in either the presence (for  $t_+$ ) or absence ( $t_-$ ) of cAMP. This mirrors the strategy used by  
406 [Kuhlman et al. \(2007\)](#), and the validity of this approach is attested to by the calibration data shown  
407 in Appendix 2 Figure 1. However, controlling *in vivo* TF activity using small molecules has many  
408 limitations. Most TFs cannot be quantitatively controlled with small molecules, and those that  
409 can often require special host strains (e.g., see [Kuhlman et al. \(2007\)](#)). Moreover, varying the *in*  
410 *vivo* concentration of a TF can affect cellular physiology in ways that can confound quantitative  
411 measurements.

## 412 Outlook

413 MPRAs performed on array-synthesized promoter libraries should be able to overcome both of  
414 these experimental limitations. Current MPRA technology is able to quantitatively measure gene  
415 expression for  $\geq 10^4$  transcriptional regulatory sequences in parallel. We estimate that this would  
416 enable the simultaneous measurement of  $\sim 10^2$  highly resolved allelic manifolds, each manifold  
417 representing a different promoter architecture. Moreover, by using array-synthesized promoters in  
418 conjunction with MPRAs, one can measure  $t_+$  and  $t_-$  by systematically altering the DNA sequence of  
419 TF binding sites, rather than relying on small molecule effectors of each TF. This capability would,  
420 among other things, enable biophysical studies of promoters that have multiple binding sites for  
421 the same TF; in such cases it might make sense to use measurement spaces having more than two  
422 dimensions.

423 Will allelic manifolds be useful for understanding transcriptional regulation in eukaryotes?  
424 Both FACS-based MPRAs ([Sharon et al., 2012](#); [Weingarten-Gabbay et al., 2017](#)) and RNA-Seq-based  
425 MPRAs ([Melnikov et al., 2012](#); [Kwasnieski et al., 2012](#); [Patwardhan et al., 2012](#)) are well established  
426 in eukaryotes so, on a technical level, experiments analogous to those described here should be  
427 feasible. The bigger question, we believe, is whether the results of such experiments would  
428 be interpretable. Eukaryotic transcriptional regulation is far more complex than transcriptional  
429 regulation in bacteria. Still, we believe that pursuing the measurement and modeling of allelic  
430 manifolds in this context is worthwhile. Despite the underlying complexities, simple “effective”  
431 biophysical models might work surprisingly well. Similar approaches might also be useful for  
432 studying other eukaryotic regulatory processes that are compatible with MPRAs, such as alternative  
433 splicing ([Wong et al., 2018](#)).

434 Based on these results, we advocate a very different approach to dissecting cis-regulatory  
435 grammar than has been pursued by other groups. Rather than attempting to identify a single  
436 quantitative model that can explain regulation by many different arrangements of TF binding sites  
437 ([Gertz et al., 2009](#); [Sharon et al., 2012](#); [Mogno et al., 2013](#); [Smith et al., 2013](#); [Levo and Segal, 2014](#);  
438 [White et al., 2016](#)), we suggest focused studies of the biophysical interactions that result from  
439 *specific* TF binding site arrangements. The measurement and modeling of allelic manifolds provides  
440 a systematic and stereotyped way of doing this. By coupling this approach with MPRAs, it should  
441 be possible to perform such studies on hundreds of systematically varied regulatory sequence  
442 architectures in parallel. General rules governing cis-regulatory grammar might then be identified  
443 empirically. We suspect that this bottom-up strategy to studying cis-regulatory grammar is likely to  
444 reveal regulatory mechanisms that would be hard to anticipate in top-down studies.

## 445 Materials and Methods

446 Appendix 1 describes the media, strains, plasmids, and promoters assayed in this work. Appendix  
447 2 describes the colorimetric  $\beta$ -galactosidase activity assay, adapted from [Lederberg \(1950\)](#) and

**Table 2.** Key resources table.

Reagent type (species) or resource	Designation	Source or reference	Identifiers	Additional information
genetic reagent ( <i>E. coli</i> )	JK10	this paper	none	genotype: $\Delta cyaA \Delta cpdA \Delta lacY \Delta lacZ \Delta dksA$
recombinant DNA reagent	pJK47.419	this paper	none	cloning vector with BsmBI cut sites, <i>ccdB</i> cassette, <i>lacZ</i> reporter gene kanamycin resistance, pSC101 origin
recombinant DNA reagent	pJK48 & variants	this paper	none	reporter plasmids cloned from pJK47.419
chemical compound	cAMP	Sigma-Aldrich	A9501-1G	Adenosine 3',5'-cyclic monophosphate, 1 gram
chemical compound	IPTG	Sigma-Aldrich	I5502-1G	Isopropyl $\beta$ -D-1-thiogalactopyranoside, 1 gram
chemical compound	ONPG	Sigma-Aldrich	N1127-5G	2-Nitrophenyl $\beta$ -D-galactopyranoside, 5 gram
commercial assay or kit	PureLink Genomic DNA Mini Kit	ThermoFisher	K182001	none
commercial assay or kit	Nextera XT DNA Library Preparation Kit	Illumina	FC-131-1024	24 samples
other	RDM	Teknova	M2105	growth media: MOPS EZ Rich Defined Medium Kit, 5 liter
other	PopCulture Reagent	MilliporeSigma	71092-4	75 milliliters
other	Breathe-Easier film	USA Scientific	9123-6100	sterile, 100 per box
other	Epoch 2 Microplate Spectrophotometer	BioTek	EPOCH2C	none
software	analysis scripts	this paper	none	Available at <a href="https://github.com/jbkinney/17_inducibility">github.com/jbkinney/17_inducibility</a>

448 *Miller (1972)*, that was used to measure expression levels. Appendix 3 provides details about how  
 449 quantitative models were fit to these measurements, as well as how uncertainties in estimated  
 450 parameters were computed. Supplemental File 1 is an Excel spreadsheet containing the DNA  
 451 sequences of all assayed promoters, all  $t_+$  and  $t_-$  measurements used in this work, and all of the  
 452 parameter values fit to these data, both with and without bootstrap resampling.

### 453 **Supplementary Material**

#### 454 **Supplementary File 1**

455 Supplemental File 1 is an Excel workbook containing all of the numerical results plotted in the  
 456 Figures and listed in Table 1. Please refer to the 'overview' sheet within this workbook for a  
 457 description of each data sheet therein.

### 458 **Acknowledgments**

459 We thank Stirling Churchman, Barak Cohen, David McCandlish, Bryce Nickels, and Saurabh Sinha  
 460 for helpful discussions. We also thank Naama Barkai, Ulrich Gerland, Richard Neher, and one  
 461 anonymous referee for reviewing this manuscript and providing helpful feedback. This work was  
 462 supported by a CSHL/Northwell Health Alliance grant to JBK and by NIH Cancer Center Support  
 463 Grant 5P30CA045508.

## 464 **References**

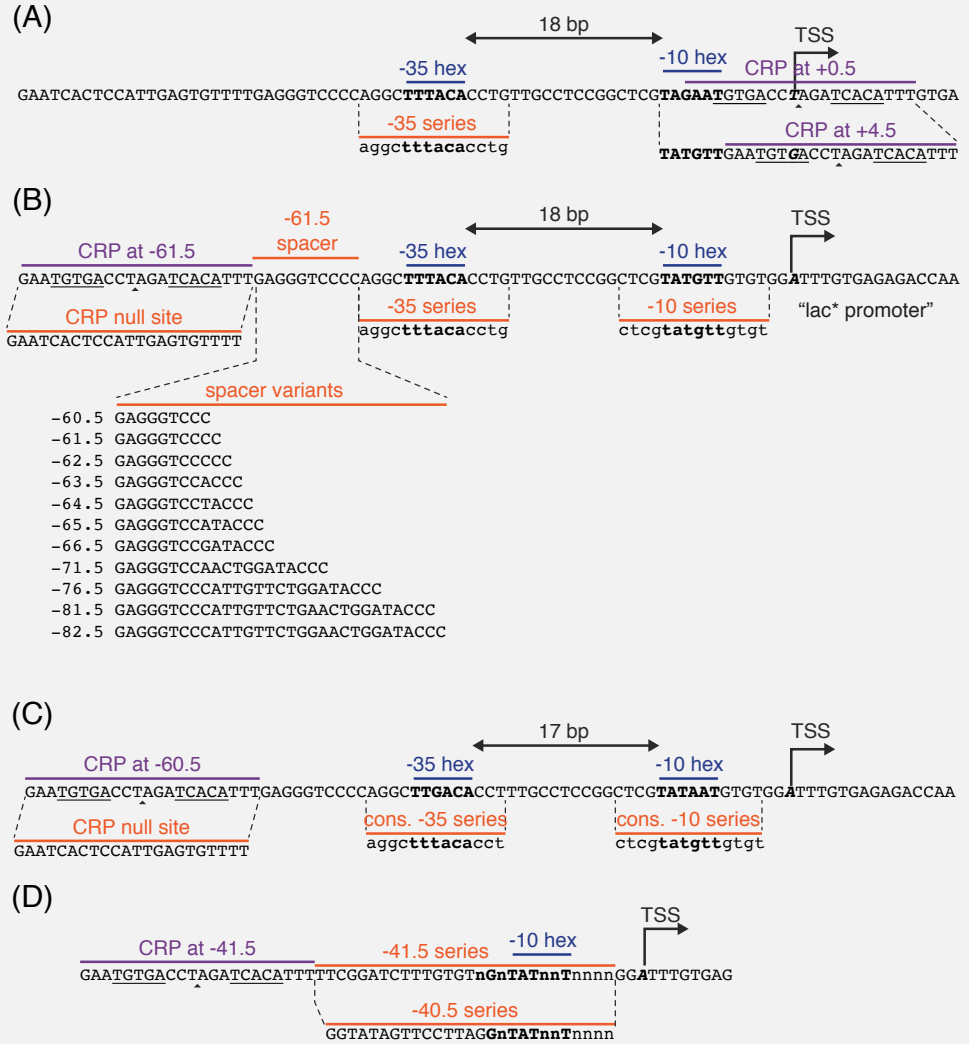
- 465 **Ackers G**, Johnson A, Shea M. Quantitative model for gene regulation by lambda phage repressor. *Proc Natl*  
466 *Acad Sci U S A*. 1982 Feb; 79(4):1129–1133.
- 467 **Adhya S**. The lac and gal operons today. *Regulation of Gene Expression in Escherichia coli*. 1996; p. 1–20.
- 468 **Beckwith J**, Grodzicker T, Arditti R. Evidence for two sites in the lac promoter region. *J Mol Biol*. 1972 Aug;  
469 69(1):155–160.
- 470 **Belliveau NM**, Barnes SL, Ireland WT, Jones DL, Sweredoski MJ, Moradian A, Hess S, Kinney JB, Phillips R.  
471 Systematic approach for dissecting the molecular mechanisms of transcriptional regulation in bacteria. *Proc*  
472 *Natl Acad Sci USA*. 2018 May; 115(21):E4796–E4805.
- 473 **Bintu L**, Buchler NE, Garcia HG, Gerland U, Hwa T, Kondev J, Phillips R. Transcriptional regulation by the numbers:  
474 models. *Curr Opin Genet Dev*. 2005 Apr; 15(2):116–124.
- 475 **Brewster RC**, Jones DL, Phillips R. Tuning promoter strength through RNA polymerase binding site design in  
476 *Escherichia coli*. *PLoS Comput Biol*. 2012; 8(12):e1002811.
- 477 **Brewster RC**, Weinert FM, Garcia HG, Song D, Rydenfelt M, Phillips R. The transcription factor titration effect  
478 dictates level of gene expression. *Cell*. 2014 Mar; 156(6):1312–1323.
- 479 **Browning DF**, Busby SJW. Local and global regulation of transcription initiation in bacteria. *Nat Rev Microbiol*.  
480 2016 Oct; 14(10):638–650.
- 481 **Busby S**, Ebright RH. Transcription activation by catabolite activator protein (CAP). *J Mol Biol*. 1999 Oct;  
482 293(2):199–213.
- 483 **Courey AJ**. *Mechanisms in transcriptional regulation*. Malden, MA: Blackwell; 2008.
- 484 **Cui L**, Murchland I, Shearwin KE, Dodd IB. Enhancer-like long-range transcriptional activation by  $\lambda$  CI-mediated  
485 DNA looping. *Proc Natl Acad Sci USA*. 2013 Feb; 110(8):2922–2927.
- 486 **Ebright RH**, Ebright YW, Gunasekera A. Consensus DNA site for the *Escherichia coli* catabolite gene activator  
487 protein (CAP): CAP exhibits a 450-fold higher affinity for the consensus DNA site than for the *E. coli* lac DNA  
488 site. *Nucl Acids Res*. 1989 Dec; 17(24):10295–10305.
- 489 **Einav T**, Duque J, Phillips R. Theoretical analysis of inducer and operator binding for cyclic-AMP receptor protein  
490 mutants. *PLoS ONE*. 2018; 13(9):e0204275.
- 491 **Foat B**, Morozov A, Bussemaker H. Statistical mechanical modeling of genome-wide transcription factor  
492 occupancy data by MatrixREDUCE. *Bioinformatics*. 2006 Jul; 22(14):e141–9.
- 493 **Garcia HG**, Phillips R. Quantitative dissection of the simple repression input-output function. *Proc Natl Acad Sci*  
494 *USA*. 2011 Jul; 108(29):12173–12178.
- 495 **Gaston K**, Bell A, Kolb A, Buc H, Busby S. Stringent spacing requirements for transcription activation by CRP.  
496 *Cell*. 1990 Aug; 62(4):733–743.
- 497 **Gertz J**, Siggia ED, Cohen BA. Analysis of combinatorial cis-regulation in synthetic and genomic promoters.  
498 *Nature*. 2009 Jan; 457(7226):215–218.
- 499 **Gunasekera A**, Ebright Y, Ebright R. DNA sequence determinants for binding of the *Escherichia coli* catabolite  
500 gene activator protein. *J Biol Chem*. 1992 Jul; 267(21):14713–14720.
- 501 **Keseler IM**, Collado-Vides J, Santos-Zavaleta A, Peralta-Gil M, Gama-Castro S, Muñiz-Rascado L, Bonavides-  
502 Martinez C, Paley S, Krummenacker M, Altman T, Kaipa P, Spaulding A, Pacheco J, Latendresse M, Fulcher  
503 C, Sarker M, Shearer AG, Mackie A, Paulsen I, Gunsalus RP, et al. EcoCyc: a comprehensive database of  
504 *Escherichia coli* biology. *Nucl Acids Res*. 2011; 39(Database issue):D583–90.
- 505 **Kinney JB**, Murugan A, Callan CG, Cox EC. Using deep sequencing to characterize the biophysical mechanism of  
506 a transcriptional regulatory sequence. *Proc Natl Acad Sci USA*. 2010 May; 107(20):9158–9163.
- 507 **Kuhlman T**, Zhang Z, Saier MH, Hwa T. Combinatorial transcriptional control of the lactose operon of *Escherichia*  
508 *coli*. *Proc Natl Acad Sci USA*. 2007 Apr; 104(14):6043–6048.

- 509 **Kwasnieski JC**, Mogno I, Myers CA, Corbo JC, Cohen BA. Complex effects of nucleotide variants in a mammalian  
510 cis-regulatory element. *Proc Natl Acad Sci USA*. 2012 Nov; 109(47):19498–19503.
- 511 **Lederberg J**. The beta-d-galactosidase of *Escherichia coli*, strain K-12. *J Bacteriol*. 1950; 60(4):381–392.
- 512 **Lee DJ**, Minchin SD, Busby SJW. Activating transcription in bacteria. *Annu Rev Microbiol*. 2012; 66(1):125–152.
- 513 **Levo M**, Segal E. In pursuit of design principles of regulatory sequences. *Nat Rev Genet*. 2014 Jul; 15(7):453–468.
- 514 **Malan T**, Kolb A, Buc H, McClure W. Mechanism of CRP-cAMP activation of lac operon transcription initiation  
515 activation of the P1 promoter. *J Mol Biol*. 1984 Dec; 180(4):881–909.
- 516 **Markovitch O**, Agmon N. Structure and energetics of the hydronium hydration shells. *J Phys Chem A*. 2007  
517 Mar; 111(12):2253–2256.
- 518 **McClure WR**, Hawley DK, Youderian P, Susskind MM. DNA determinants of promoter selectivity in *Escherichia*  
519 *coli*. *Cold Spring Harb Symp Quant Biol*. 1983; 47 Pt 1:477–481.
- 520 **Melnikov A**, Murugan A, Zhang X, Tesileanu T, Wang L, Rogov P, Feizi S, Gnirke A, Callan CG, Kinney JB, Kellis M,  
521 Lander ES, Mikkelsen TS. Systematic dissection and optimization of inducible enhancers in human cells using  
522 a massively parallel reporter assay. *Nat Biotechnol*. 2012 Feb; 30(3):271–277.
- 523 **Miller J**. *Experiments in Molecular Genetics*. Cold Spring Harbor, NY: Cold Spring Harbor Laboratory Press;  
524 1972.
- 525 **Mogno I**, Kwasnieski JC, Cohen BA. Massively parallel synthetic promoter assays reveal the in vivo effects of  
526 binding site variants. *Genome Res*. 2013 Nov; 23(11):1908–1915.
- 527 **Morita T**, Shigesada K, Kimizuka F, Aiba H. Regulatory effect of a synthetic CRP recognition sequence placed  
528 downstream of a promoter. *Nucl Acids Res*. 1988 Aug; 16(15):7315–7332.
- 529 **Neidhardt FC**, Bloch PL, Smith DF. Culture medium for enterobacteria. *J Bacteriol*. 1974 Sep; 119(3):736–747.
- 530 **Niu W**, Kim Y, Tau G, Heyduk T, Ebricht RH. Transcription activation at class II CAP-dependent promoters: two  
531 interactions between CAP and RNA polymerase. *Cell*. 1996 Dec; 87(6):1123–1134.
- 532 **Parkinson G**, Wilson C, Gunasekera A, Ebricht YW, Ebricht RH, Ebricht RE, Berman HM. Structure of the CAP-DNA  
533 complex at 2.5 angstroms resolution: a complete picture of the protein-DNA interface. *J Mol Biol*. 1996 Jul;  
534 260(3):395–408.
- 535 **Patwardhan RP**, Hiatt JB, Witten DM, Kim MJ, Smith RP, May D, Lee C, Andrie JM, Lee SI, Cooper GM, Ahituv N,  
536 Pennacchio LA, Shendure J. Massively parallel functional dissection of mammalian enhancers in vivo. *Nat*  
537 *Biotechnol*. 2012 Feb; 30(3):265–270.
- 538 **Pribnow D**. Nucleotide sequence of an RNA polymerase binding site at an early T7 promoter. *Proc Natl Acad*  
539 *Sci USA*. 1975 Mar; 72(3):784–788.
- 540 **Ptashne M**, Gann A. *Genes and signals*. Cold Spring Harbor, NY: Cold Spring Harbor Laboratory Press; 2002.
- 541 **Ptashne M**. Regulated recruitment and cooperativity in the design of biological regulatory systems. *Philos*  
542 *Transact A Math Phys Eng Sci*. 2003 Jun; 361(1807):1223–1234.
- 543 **Reznikoff WS**. The lactose operon-controlling elements: a complex paradigm. *Mol Microbiol*. 1992 Sep;  
544 6(17):2419–2422.
- 545 **Rhodus VA**, West DM, Webster CL, Busby SJ, Savery NJ. Transcription activation at class II CRP-dependent  
546 promoters: the role of different activating regions. *Nucl Acids Res*. 1997 Jan; 25(2):326–332.
- 547 **Roy S**, Garges S, Adhya S. Activation and repression of transcription by differential contact: two sides of a coin. *J*  
548 *Biol Chem*. 1998 Jun; 273(23):14059–14062.
- 549 **Salgado H**, Peralta-Gil M, Gama-Castro S, Santos-Zavaleta A, Muñoz-Rascado L, García-Sotelo JS, Weiss V, Solano-  
550 Lira H, Martínez-Flores I, Medina-Rivera A, Salgado-Orsorio G, Alquicira-Hernández S, Alquicira-Hernández K,  
551 López-Fuentes A, Porrón-Sotelo L, Huerta AM, Bonavides-Martinez C, Balderas-Martínez YI, Pannier L, Olvera  
552 M, et al. RegulonDB v8.0: omics data sets, evolutionary conservation, regulatory phrases, cross-validated gold  
553 standards and more. *Nucl Acids Res*. 2013 Jan; 41(Database issue):D203–13.

- 554 **Schmidt A**, Kochanowski K, Vedelaar S, Ahrné E, Volkmer B, Callipo L, Knoops K, Bauer M, Aebersold R, Heine-  
555 mann M. The quantitative and condition-dependent Escherichia coli proteome. *Nat Biotechnol.* 2016 Jan;  
556 34(1):104–110.
- 557 **Sharon E**, Kalma Y, Sharp A, Raveh-Sadka T, Levo M, Zeevi D, Keren L, Yakhini Z, Weinberger A, Segal E. Infer-  
558 ring gene regulatory logic from high-throughput measurements of thousands of systematically designed  
559 promoters. *Nat Biotechnol.* 2012 May; 30(6):521–530.
- 560 **Shea MA**, Ackers GK. The OR control system of bacteriophage lambda. A physical-chemical model for gene  
561 regulation. *J Mol Biol.* 1985 Jan; 181(2):211–230.
- 562 **Sherman MS**, Cohen BA. Thermodynamic state ensemble models of cis-regulation. *PLoS Comput Biol.* 2012;  
563 8(3):e1002407.
- 564 **Smith RP**, Taher L, Patwardhan RP, Kim MJ, Inoue F, Shendure J, Ovcharenko I, Ahituv N. Massively parallel  
565 decoding of mammalian regulatory sequences supports a flexible organizational model. *Nat Genet.* 2013  
566 Sep; 45(9):1021–1028.
- 567 **So Lh**, Ghosh A, Zong C, Sepúlveda LA, Segev R, Golding I. General properties of transcriptional time series in  
568 Escherichia coli. *Nature Genetics.* 2011 Jun; 43(6):554–560.
- 569 **Spitz F**, Furlong EEM. Transcription factors: from enhancer binding to developmental control. *Nat Rev Genet.*  
570 2012 Sep; 13(9):613–626.
- 571 **Thompson MG**, Sedaghatian N, Barajas JF, Wehrs M, Bailey CB, Kaplan N, Hillson NJ, Mukhopadhyay A, Keasling  
572 JD. Isolation and characterization of novel mutations in the pSC101 origin that increase copy number. *Sci Rep.*  
573 2018 Jan; 8(1):1590.
- 574 **Ushida C**, Aiba H. Helical phase dependent action of CRP: effect of the distance between the CRP site and the  
575 -35 region on promoter activity. *Nucl Acids Res.* 1990 Nov; 18(21):6325–6330.
- 576 **Vilar JMG**, Leibler S. DNA looping and physical constraints on transcription regulation. *J Mol Biol.* 2003 Aug;  
577 331(5):981–989.
- 578 **Weingarten-Gabbay S**, Nir R, Lubliner S, Sharon E, Kalma Y, Weinberger A, Segal E. Deciphering transcriptional  
579 regulation of human core promoters. *bioRxiv.* 2017 Aug; .
- 580 **White MA**, Kwasnieski JC, Myers CA, Shen SQ, Corbo JC, Cohen BA. A Simple Grammar Defines Activating and  
581 Repressing cis-Regulatory Elements in Photoreceptors. *Cell Rep.* 2016 Oct; 17(5):1247–1254.
- 582 **Wong MS**, Kinney JB, Krainer AR. Quantitative Activity Profile and Context Dependence of All Human 5' Splice  
583 Sites. *Mol Cell.* 2018 Aug; 71(6):1012–1026.e3.

584 **Appendix 1**

585 **Media, Strains, Plasmids, and Promoters**



586

587

588

589

590

591

592

593

594

595

596

**Appendix 1 Figure 1.** Promoter sequences used in this study. In all panels, the -35 and -10 hexamers of the RNAP binding site are in bold. CRP binding site centers are indicated by small triangles. The palindromic pentamers of the core CRP binding site in each construct are underlined. The transcription start site (TSS) is bold and italicized. Lowercase bases ('a', 'c', 'g', and 't') indicate positions synthesized with a 24% mutation rate. The lowercase character 'n' indicates completely randomized positions. (A) Occlusion promoters assayed for Main Text Figure 2. (B) Class I promoters assayed for Main Text Figure 5. In the main text we refer to the wild-type promoter with CRP at -61.5 bp as the lac\* promoter. The lac\* promoter served as the template for all of the promoters shown here. (C) Strong class I promoters assayed for Main Text Figure 8. (D) Class II promoters assayed for Main Text Figure 9.

Expression measurements were performed on cells grown in rich defined media (RDM; purchased from Teknova) (*Neidhardt et al., 1974*) supplemented with 10 mM NaHCO<sub>3</sub>, 1

598

599

600

601

602

mM IPTG (Sigma), and 0.2% glucose. We refer to this media as RDM'. RDM' was further supplemented with 50  $\mu$ g/ml kanamycin (Sigma) when growing cells, as well as 250  $\mu$ M cAMP (Sigma) when measuring  $t_+$ .

603

604

605

606

607

608

609

610

611

612

613

614

615

616

Expression measurements were performed in *E. coli* strain JK10, which has genotype  $\Delta cyaA \Delta cpdA \Delta lacY \Delta lacZ \Delta dksA$ . JK10 is derived from strain TK310 (Kuhlman *et al.*, 2007), which is  $\Delta cyaA \Delta cpdA \Delta lacY$ . The  $\Delta cyaA \Delta cpdA$  mutations prevent TK310 from synthesizing or degrading cAMP, thus allowing *in vivo* cAMP concentrations to be quantitatively controlled by adding cAMP to the growth media. Into TK310 we introduced the  $\Delta lacZ$  mutation, yielding strain DJ33; this mutation enables the use of  $\beta$ -galactosidase activity assays for measuring plasmid-based *lacZ* expression. In our initial experiments, we found that the growth rate of DJ33 in RDM' varied strongly with the amount of cAMP added to the media. Fortunately, we isolated a spontaneous knock-out mutation in *dksA* (thus yielding JK10), which caused the growth rate ( $\sim 30$  min doubling time) in RDM' to be independent of cAMP concentrations below  $\sim 500 \mu$ M.<sup>a</sup> The TK310, DJ33, and JK10 genotypes were confirmed by whole genome sequencing using the PureLink Genomic DNA Mini Kit (ThermoFisher) for extracting genomic DNA from cultured cells and the Nextera XT DNA Library Preparation Kit (Illumina) for preparing whole-genome sequencing libraries.

Expression of the *lacZ* gene was driven from variants of a plasmid we call pJK48. These reporter constructs were cloned as follows. We started with the vector pJK14 from Kinney *et al.* (2010). pJK14 contains a pSC101 origin of replication ( $\sim 5$  copies per cell; Thompson *et al.* (2018)), a kanamycin resistance gene, and a *ccdB* cloning cassette positioned immediately upstream of a *gfpmut2* reporter gene and flanked by outward-facing BsmBI restriction sites. First, the *gfpmut2* gene in this vector was replaced with *lacZ*, yielding pJK47. Next, the ribosome binding site in the 5' UTR of *lacZ* was weakened, yielding pJK47.419; this weakening prevents *lacZ* expression from substantially slowing cell growth in RDM'. pJK47.419 was propagated in DB3.1 *E. coli* (Invitrogen), which is resistant to the CcdB toxin. The promoters we assayed were variants of what we call the "lac\*" promoter. The lac\* promoter is similar to the endogenous *lac* promoter of *E. coli* MG1655 except for (i) it contains a CRP binding site with a consensus right pentamer and (ii) it contains mutations that were introduced in an effort to remove previously reported cryptic promoters (Reznikoff, 1992). Promoter-containing insertion cassettes were created through overlap-extension PCR and flanked by outward-facing BsaI restriction sites. All primers were ordered from Integrated DNA Technologies. Note that some of the primers used to create these inserts were synthesized using pre-mixed phosphoramidites at specified positions; this is how a 24% mutation rate in the -10 or -35 regions of the RNAP binding site was achieved. The resulting promoter sequences are illustrated in Appendix 1 Figure 1. To clone variants of pJK48, we separately digested the pJK47.419 vector with BsmBI (NEB) and the appropriate insert with BsaI (NEB). Digests were then cleaned up (Qiagen PCR purification kit) and ligated together in at 1:1 molar ratio for 1 hour using T4 DNA ligase (Invitrogen). After 90 min dialysis, plasmids were transformed into electrocompetent JK10 cells. Individual clones were plated on LB supplemented with kanamycin (50  $\mu$ g/ml). After initial cloning and plating, each colony was re-streaked, grown in LB+kan, and stored as a catalogued glycerol stock. The promoter region of each clone was sequenced in both directions. Only plasmids with validated promoter sequences were used for the measurements presented in this paper. The promoter sequences of all 448 plasmids used in this study, as well as their measured  $t_+$  and  $t_-$  values, are provided at

640

641

bioRxiv preprint

642

643

644

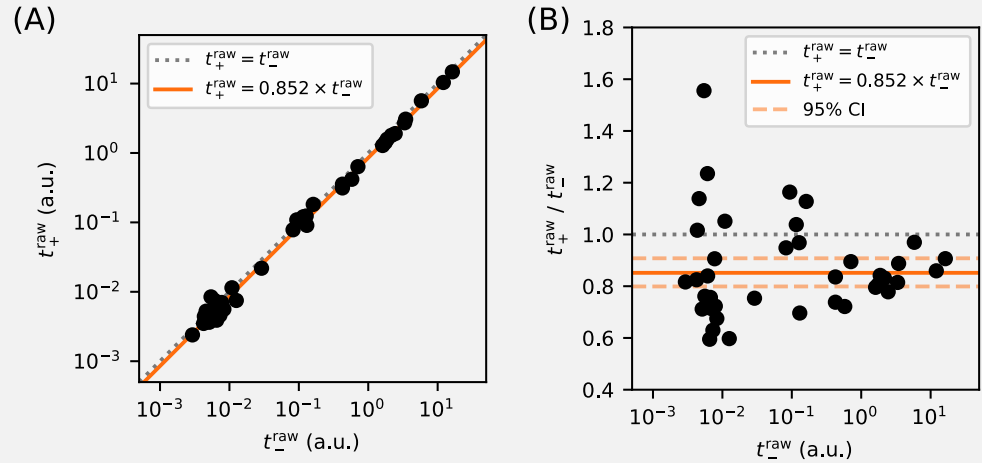
645

[https://github.com/jbkinney/17\\_inducibility](https://github.com/jbkinney/17_inducibility).

<sup>a</sup>We note that JK10 will not grow in minimal media in the absence of cAMP.

646 Appendix 2

647 Miller assays and the calibration of expression measurements



648

649

650 **Appendix 2 Figure 1.** Calibration of expression measurements with and without cAMP. (A)  
651 Measurements of  $t_+^{\text{raw}}$  (in 250  $\mu\text{M}$  cAMP) vs  $t_-^{\text{raw}}$  (in 0  $\mu\text{M}$  cAMP) for promoters in which the CRP binding  
652 site has been replaced by a non-functional “null” site. As expected, these data lie close to the  $t_+^{\text{raw}} = t_-^{\text{raw}}$   
653 diagonal (dotted line). (B) Upon closer inspection, however, we found that  $t_+^{\text{raw}}$  values consistently fell  
654 slightly below corresponding  $t_-^{\text{raw}}$  values. Using least-squares fitting we found that, on average,  
655  $t_+^{\text{raw}}/t_-^{\text{raw}} = 0.852^{+0.056}_{-0.053}$  where uncertainties indicate a 95% confidence interval (reflecting 1.96 times the  
656 standard error of the mean in log space). To correct for this bias, we plot and fit models to  $t_+ = t_+^{\text{raw}}$  and  
657  $t_- = 0.855 \times t_-^{\text{raw}}$  throughout this paper.

659

660

661

662

663

664

665

666

667

668

669

We obtained  $t_+$  and  $t_-$  measurements for each promoter as follows. First, the corresponding *E. coli* clone was streaked out on LB+kan agar and grown overnight. A colony was then picked and used to inoculate a 1.5 ml overnight LB+kan liquid culture. Either 8  $\mu\text{l}$ , 6  $\mu\text{l}$ , or 4  $\mu\text{l}$  of the overnight culture were then diluted into 200  $\mu\text{l}$  RDM'+kan. 25  $\mu\text{l}$  of each dilution was then added to 175  $\mu\text{l}$  RDM'+kan in a 96-well optical bottom plate and supplemented with either 0  $\mu\text{M}$  cAMP (for  $t_-^{\text{raw}}$ ), 250  $\mu\text{M}$  cAMP (for  $t_+^{\text{raw}}$ ), or another cAMP concentration (for some  $t_+^{\text{raw}}$  measurements in Figure 3). The plate was then covered with Breathe-Easier film (USA Scientific) and cells were cultured for  $\sim 3$  hr at 37  $^\circ\text{C}$ , shaking at 900 RPM in a microplate shaker. During this time, 5.5 ml of lysis buffer was freshly prepared using 1.5 ml RDM', 4.0 ml PopCulture reagent (Millipore), 114  $\mu\text{l}$  of 35 mg/ml chloramphenicol (Sigma), and 44  $\mu\text{l}$  of 40 U/ $\mu\text{l}$  rLysozyme (Sigma).

Microplate film was removed and cell density (quantified by  $A_{600}$ ) was measured using an Epoch 2 Microplate Spectrophotometer (BioTek). Cells were then lysed by adding 25  $\mu\text{l}$  lysis buffer to each microplate well, incubating the microplate at room temperature for 10 minutes without shaking, then cooling the microplate at 4  $^\circ\text{C}$  for a minimum of 15 minutes. In each well of a 96-well optical bottom plate, 50  $\mu\text{l}$  of lysate was then added to 50  $\mu\text{l}$  of pre-chilled Z-buffer containing 1 mg/ml ONPG (Sigma). Samples were sealed with optical film and both  $A_{420}$  and  $A_{550}$  were periodically measured in the plate reader over an extended

672

673

bioRxiv preprint

674

675

676

677

period of time (every 1.5 min for 1 hour or every 15 min for 10 hours, depending on the level of expression expected).

678

679

The raw expression levels were quantified from these absorbance data using the formula

680

681

$$t_{\pm}^{\text{raw}} = \frac{\Delta A_{420} - \Delta A_{550}}{V \cdot \Delta T \cdot A_{600}}, \quad (9)$$

682

683

684

685

686

687

688

689

690

691

692

693

694

where  $V = 50$  is the volume of lysate in  $\mu\text{l}$  added to the ONPG reaction,  $\Delta T$  is the change in time from the beginning of the measurement, and  $\Delta A_X$  indicates a change in absorbance at  $X$  nm over this time interval. Only data from wells with  $A_{600} \lesssim 0.5$  were analyzed. Note that the  $A_{550}$  term in Equation 9 is not multiplied by 1.75 as it is in [Miller \(1972\)](#). This is because our  $A_{550}$  measurements are used to compensate for condensation on the microplate film, not cellular debris as in [Miller \(1972\)](#); our lysis procedure produces no detectable cellular debris. In practice, Equation 9 was not evaluated using individual measurements, but was computed from the slope of a line fit to all of the non-saturated absorbance measurements. Raw  $A_{420}$ ,  $A_{550}$ , and  $A_{600}$  values, as well as our analysis scripts, are available at [https://github.com/jbkinney/17\\_inducibility](https://github.com/jbkinney/17_inducibility). Median values from at least 3 independent Miller measurements (and often more) were used to define each measurement shown in Main Text figures.

695

696

697

698

699

700

701

702

703

704

Because we controlled the *in vivo* activity of CRP by supplementing media with or without cAMP, we tested whether CRP-independent promoters produce measurements that vary between these growth conditions. Specifically, we measured  $t_{-}^{\text{raw}}$  (in 0  $\mu\text{M}$  cAMP) and  $t_{+}^{\text{raw}}$  (in 250  $\mu\text{M}$  cAMP) for 39 promoters in which the CRP binding site was replaced with a “null” site (see Appendix 1, Figures 1B and 1C). These measurements are potted in Figure 1 of this Appendix, and show a slight bias. To correct for this bias, we use an unadjusted  $t_{+} = t_{+}^{\text{raw}}$  together with an adjusted  $t_{-} = 0.855 \times t_{-}^{\text{raw}}$  throughout the main text. Note that  $t_{+} = t_{+}^{\text{raw}}$  was used for all nonzero cAMP concentrations, including those in Main Text Figure 3B that differ from 250  $\mu\text{M}$ . Some upward bias is therefore possible in these  $t_{+}$  measurements, but we do not expect this to greatly affect our conclusions.

705 **Appendix 3**

707 **Parameter inference**

708 Allelic manifold parameters were fit to measured  $t_+$  and  $t_-$  values as follows. First, outlier  
 709 data points were called by eye and excluded from the parameter fitting procedure. We  
 710 denote the remaining measurements using  $t_+^{i,\text{data}}$  and  $t_-^{i,\text{data}}$ , where  $i = 1, 2, \dots, n$  indexes the  $n$   
 711 non-outlier data points. Corresponding model predictions  $t_+^i(\theta)$  and  $t_-^i(\theta)$ , where  $\theta$  denotes  
 712 model parameters, were then fit to these data using nonlinear least squares optimization.  
 713 Specifically, we inferred parameters  $\theta^* = \text{argmin}_\theta \mathcal{L}(\theta)$  where the loss function is given by

$$714 \mathcal{L}(\theta) = \sum_{i=1}^n \left( \left[ \log \frac{t_+^i(\theta)}{t_+^{i,\text{data}}} \right]^2 + \left[ \log \frac{t_-^i(\theta)}{t_-^{i,\text{data}}} \right]^2 \right). \quad (10)$$

715 These optimal parameter values  $\theta^*$  were used to generate the best-estimate allelic mani-  
 716 folds, which are plotted in black in Main Text figures. Uncertainties in  $\theta$  were estimated by  
 717 performing the same inference procedure on bootstrap-resampled data. For each variable  
 718  $X \in \{F, P, \alpha', \beta', t_{\text{sat}}, t_{\text{bg}}\}$ , we report

$$719 X = (X_{50})^{+(X_{84}-X_{50})} (X_{50})^{-(X_{50}-X_{16})} \quad (11)$$

720 where  $X_{50}, X_{84}$ , and  $X_{16}$  respectively denote the median, 84th percentile, and 16th percentile  
 721 of  $X$  values obtained from bootstrap resampling. In the case of  $X \in \{F, P, \alpha\}$ , we also report

$$722 \Delta G_X = -k_B T \log X_{50} \pm k_B T \left( \frac{\log X_{84} - \log X_{16}}{2} \right), \quad (12)$$

723 where  $1 \text{ kcal/mol} = 1.62 k_B T$ , corresponding to  $37^\circ\text{C}$ . We now describe each specific inference  
 724 procedure in more detail.

725 **Inference for Main Text Figure 2B**

726 We inferred  $\theta = \{t_{\text{sat}}, t_{\text{bg}}, F, P_1, P_2, \dots, P_n\}$ , with model predictions given by

$$727 t_+^i(\theta) = t_{\text{sat}} \frac{P_i}{1 + F + P_i} + t_{\text{bg}}, \quad t_-^i(\theta) = t_{\text{sat}} \frac{P_i}{1 + P_i} + t_{\text{bg}}. \quad (13)$$

728 Parameters were fit to the  $n = 39$  non-outlier measurements made for promoters with +0.5  
 729 bp or +4.5 bp architecture. We found that  $F = 23.9_{-2.5}^{+3.1}$  and  $t_{\text{bg}} = 2.30 \times 10^{-3}$  a.u., while  $t_{\text{sat}}$   
 730 values remained highly uncertain.

731 **Inference for Main Text Figure 3B**

732 We performed a separate inference procedure for each of the seven cAMP concentra-  
 733 tions  $C \in \{250, 125, 50, 25, 10, 5, 2.5\}$ , indicated in  $\mu\text{M}$  units. Specifically, we inferred  $\theta_C =$   
 734  $\{F_C, P_1, P_2, \dots, P_{n_C}\}$  where  $n_C$  is the number of promoters for which  $t_+$  was measured using  
 735 cAMP concentration  $C$ . Model predictions were given by

$$736 t_+^i(\theta_C) = t_{\text{sat}} \frac{P_i}{1 + F_C + P_i} + t_{\text{bg}}, \quad t_-^i(\theta_C) = t_{\text{sat}} \frac{P_i}{1 + P_i} + t_{\text{bg}}, \quad (14)$$

737 where  $t_{\text{sat}} = 15.1$  a.u. is the median saturated transcription rate from Main Text Figure 5C,  
 738 and  $t_{\text{bg}} = 2.30 \times 10^{-3}$  a.u. is the median background transcription rate from Main Text Fig. 2B.  
 739 Note that many of the  $t_-^i$  measurements were used in the inference procedures for multiple  
 740 values of  $C$ , whereas each  $t_+^i$  measurement was used in only one such inference procedure.

751

### Inference for Main Text Figure 5B

752

Using data from both the -10 and -35 allelic series for the -61.5 bp promoter architecture, we inferred  $\theta = \{t_{\text{sat}}, t_{\text{bg}}, \alpha', P_1, \dots, P_n\}$ . Model predictions were given by

753

754

755

756

$$t_+^i(\theta) = t_{\text{sat}} \frac{\alpha' P_i}{1 + \alpha' P_i} + t_{\text{bg}}, \quad t_-^i(\theta) = t_{\text{sat}} \frac{P_i}{1 + P_i} + t_{\text{bg}}. \quad (15)$$

757

For each inferred  $\alpha'$ , a value for  $\alpha$  was computed using  $\alpha = \alpha'(1 + F^{-1}) - F^{-1}$ , where  $F = 23.9$  is the median CRP binding factor inferred for Main Text Figure 2B.

758

759

### Inference for Main Text Figure 5C

760

In a single fitting procedure, we inferred  $\theta = \{t_{\text{sat}}, t_{\text{bg}}^{-82.5}, \dots, t_{\text{bg}}^{-60.5}, \alpha'_{-82.5}, \dots, \alpha'_{-60.5}, P_1, \dots, P_n\}$  using

761

762

763

764

$$t_+^i(\theta) = t_{\text{sat}} \frac{\alpha'_{D_i} P_i}{1 + \alpha'_{D_i} P_i} + t_{\text{bg}}^{D_i}, \quad t_-^i(\theta) = t_{\text{sat}} \frac{P_i}{1 + P_i} + t_{\text{bg}}^{D_i}. \quad (16)$$

765

where each  $D_i \in \{-82.5, -81.5, -76.5, -72.5, -71.5, -66.5, -65.5, -64.5, -63.5, -62.5, -61.5, -60.5\}$  represents the position of the CRP binding site (in bp relative to the TSS) for promoter  $i$ . Note that a single value for  $t_{\text{sat}}$  was inferred for all promoter architectures, while both  $t_{\text{bg}}^D$  and  $\alpha'_D$  varied with CRP position  $D$ . The corresponding values of  $\alpha$  plotted in Main Text Figure 5D and listed in Main Text Table 2 were computed using  $\alpha_D = \alpha'_D(1 + F^{-1}) - F^{-1}$  where  $F = 23.9$  is the median CRP binding factor inferred for Main Text Figure 2B. Among other results, we find that  $t_{\text{sat}} = 15.1_{-0.5}^{+0.6}$  a.u..

771

772

### Inference for Main Text Figure 8C

773

For each spacing  $D$ , we separately inferred  $\theta_D = \{\alpha'_D, \beta'_D, t_{\text{bg}}^D\}$  using

774

775

776

$$t_+^i(\theta_D) = \beta'_D t_{\text{sat}} \frac{\alpha'_D P_i}{1 + \alpha'_D P_i} + t_{\text{bg}}^D, \quad t_-^i(\theta_D) = t_{\text{sat}} \frac{P_i}{1 + P_i} + t_{\text{bg}}^D. \quad (17)$$

777

where  $t_{\text{sat}} = 15.1$  a.u. is the median saturated transcription rate inferred for Main Text Figure 5C. We then computed  $\alpha_D = \alpha'_D(1 + F^{-1}) - F^{-1}$  and  $\beta_D = \beta'_D(1 + \alpha_D^{-1} F^{-1}) - \alpha_D^{-1} F^{-1}$ , using the median CRP binding factor  $F = 23.9$  inferred for Main Text Figure 2B.

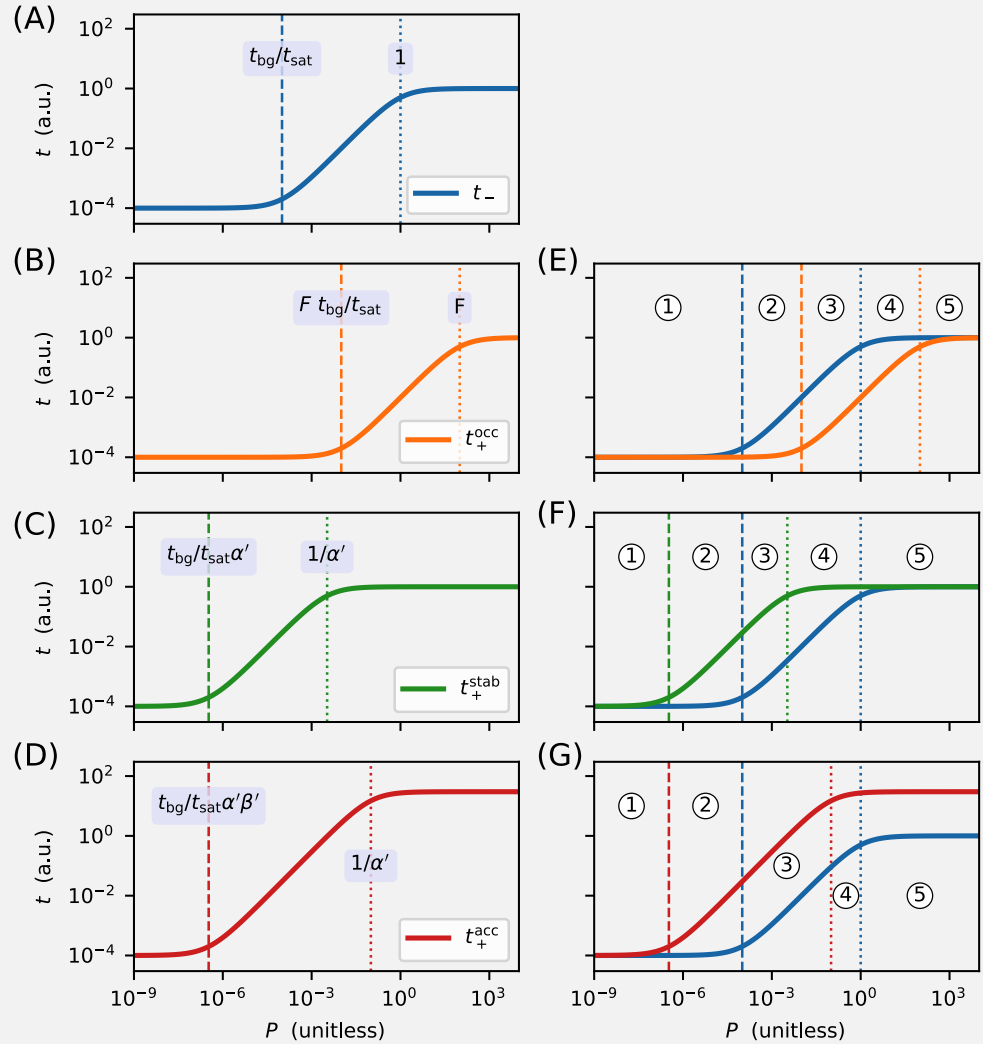
778

779

780 **Appendix 4**

781

**Derivation of allelic manifold regimes**



782

783

784

785

786

787

788

789

790

791

792

793

794

795

796

**Appendix 4 Figure 1.** Derivation of the regimes of allelic manifolds. Panels A-D show simulated induction curves for transcription  $t$  as a function of the RNAP binding factor  $P$ . Dashed lines indicate boundaries between the minimal and linear regimes of each curve, while dotted lines indicate boundaries between linear and maximal regimes. A formula for the value of  $P$  at each regime boundary is also shown. All simulations used  $t_{sat} = 1$  a.u.,  $t_{bg} = 10^{-4}$  a.u.,  $F = 100$ , and  $P$  ranging from  $10^{-9}$  to  $10^4$ . (A) Induction curve for unregulated transcription; see Equation 18. (B) Induction curve for transcription repressed by occlusion; see Equation 19. (C) Induction curve for transcription activated by stabilization ( $\alpha = 300$ ); see Equation 20. (D) Induction curve for transcription activated by acceleration ( $\alpha = 10$ ,  $\beta = 30$ ); see Equation 21. Panels E-G show how overlaps between the six regimes of two induction curves (three for  $t_-$  and three for  $t_+$ ) result in five distinct regimes for the corresponding allelic manifold. (E) Regimes of the allelic manifold for occlusion, which is shown in Fig. 1C. (F) Regimes of the allelic manifold for stabilization, which is shown in Fig. 4C. (G) Regimes of the allelic manifold for acceleration, which is shown in Fig. 7C.

798 Each transcription rate modeled in this work is a sigmoidal function of the unitless RNAP-  
 799 DNA binding factor  $P$ . As such, a log-log plot of transcription  $t$  as a function of  $P$  reveals  
 800 a sigmoidal curve having three distinct regimes. The "minimal" regime of this induction  
 801 curve comprises values of  $P$  that are sufficiently small for  $t$  to be well-approximated by  
 802 its smallest value ( $t_{bg}$  in all cases). The "maximal" regime occurs when  $P$  is so large that  $t$   
 803 is well-approximated by its largest value (either  $t_{sat}$  or  $\beta' t_{sat}$ ). Between these maximal and  
 804 minimal regimes lies a "linear" regime in which  $t$  is approximately proportional to  $P$ .

For unregulated transcription, which in this paper is denoted  $t_-$ , these three regimes are given by,

$$t_- = t_{sat} \frac{P}{1+P} + t_{bg} \approx \begin{cases} t_{bg} & \text{for } P \ll \frac{t_{bg}}{t_{sat}} \\ t_{sat} P & \text{for } \frac{t_{bg}}{t_{sat}} \ll P \ll 1 \\ t_{sat} & \text{for } 1 \ll P \end{cases} \quad (18)$$

See Figure 1A. For transcription that is repressed by occlusion (with  $F \gg 1$ ), which we denote here by  $t_+^{occ}$ , these three regimes are shifted (relative to  $t_-$ ) to larger values of  $P$  by a factor of approximately  $F$ . As a result,

$$t_+^{occ} = t_{sat} \frac{P}{1+F+P} + t_{bg} \approx \begin{cases} t_{bg} & \text{for } P \ll F \frac{t_{bg}}{t_{sat}} \\ t_{sat} \frac{P}{1+F} & \text{for } F \frac{t_{bg}}{t_{sat}} \ll P \ll F \\ t_{sat} & \text{for } F \ll P \end{cases} \quad (19)$$

See Figure 1B. By contrast, for transcription that is activated by stabilization, denoted here by  $t_+^{stab}$ , these three regimes shift (relative to  $t_-$ ) to lower values of  $P$  by a factor of  $1/\alpha'$ , giving

$$t_+^{stab} = t_{sat} \frac{\alpha' P}{1+\alpha' P} + t_{bg} \approx \begin{cases} t_{bg} & \text{for } P \ll \frac{t_{bg}}{t_{sat} \alpha'} \\ t_{sat} \alpha' P & \text{for } \frac{t_{bg}}{t_{sat} \alpha'} \ll P \ll \frac{1}{\alpha'} \\ t_{sat} & \text{for } \frac{1}{\alpha'} \ll P \end{cases} \quad (20)$$

See Figure 1C. For transcription that is activated partially by acceleration and partially by stabilization, here denoted by  $t_+^{acc}$ , two parameters govern the shape of the induction curve. As a result, the boundary between the minimal and linear regimes are shifted (relative to  $t_-$ ) to lower values of  $P$  by a factor of  $1/\alpha' \beta'$ , while the boundary between the linear regime and the maximal regime is shifted down by a factor of only  $1/\alpha'$ . As a result,

$$t_+^{acc} = \beta' t_{sat} \frac{\alpha' P}{1+\alpha' P} + t_{bg} \approx \begin{cases} t_{bg} & \text{for } P \ll \frac{t_{bg}}{t_{sat} \alpha' \beta'} \\ t_{sat} \alpha' \beta' P & \text{for } \frac{t_{bg}}{t_{sat} \alpha' \beta'} \ll P \ll \frac{1}{\alpha'} \\ t_{sat} \beta' & \text{for } \frac{1}{\alpha'} \ll P \end{cases} \quad (21)$$

See Figure 1D.

Each allelic manifold described in the main text has five distinct regimes. These arise from overlaps between the three regimes of  $t_-$  and the three regimes of  $t_+$ . Specifically, the five regimes of the allelic manifold for repression by occlusion, which are listed in Main Text Figure 1D, arise from the overlaps between the three regimes for  $t_-$  and the three regimes

830

bioRxiv preprint

831

832

833

834

835

836

837

838

for  $t_+^{\text{occ}}$ . These overlaps are indicated in Figure 1E. Similarly, the five regimes of the allelic manifold for activation by stabilization (Main Text Figure 4D) arise from the overlaps between the regimes of  $t_-$  and  $t_+^{\text{stab}}$ , illustrated in Figure 1F, while the regimes of the manifold for activation by acceleration (Main Text Figure 7D) arise from overlaps between the regimes of  $t_-$  and  $t_+^{\text{acc}}$ , illustrated in Figure 1G.